

Reverse genetics identifies proteins regulating lipid droplet biogenesis via amphipathic helices

Md. Abdulla Al Mamun^{1*}, M. Abu Reza², Md Sayeedul Islam³

¹Department of Biotechnology, The University of Tokyo, Tokyo, Japan

²Department of Genetic Engineering and Biotechnology, University of Rajshahi, Rajshahi, Bangladesh

³Department of Biological Sciences, Osaka University, Osaka, Japan

*Address correspondence to Md. Abdulla Al Mamun,

Department of Biotechnology, The University of Tokyo, Tokyo, Japan

1-1-1 Yayoi, Bunkyo-ku, Tokyo 113-8657, Japan

Email: abmamun@g.ecc.u-tokyo.ac.jp

Tel: +81-3-5841-5164

Fax: +81-3-5841-8016

Keywords: Amphipathic helix, Filamentous fungi, Gene duplication, Hydrophobicity, Lipid droplets, Reverse genetics

Abstract

Lipid droplets (LDs) are storage organelles for neutral lipids. Our knowledge about fungal LD biogenesis is limited to budding yeast. Moreover, regulation of LD in multinucleated filamentous fungi with considerable metabolic activity is unknown. Here, 19 LD-associated proteins were identified in *Aspergillus oryzae* using colocalization screening of a previously established Enhanced green fluorescent protein (EGFP) fusion proteins library. Following a functional screening, 12 candidates have been identified as lipid droplet regulating (LDR) proteins, the loss of which resulted in aberrant LD biogenesis. LDR proteins bind to LD via the insertion of the putative amphipathic helices (AHs) that were investigated using AH-disruptive mutations and subsequent imaging. Further analysis revealed that LdrA with Opi1 domain is essential for cytoplasmic and nuclear LD biogenesis via a novel AH. Phylogenetic analysis demonstrated the pattern of their evolution, which was predominantly based-on gene duplication. Our study provides substantial molecular insights into LD biogenesis and creates a breakthrough in using reverse genetics for identifying LD-regulating proteins.

Introduction

Lipid droplets (LD) are the ubiquitous cell organelle serving primarily as the reservoir of neutral lipids such as triacylglycerols (TG), and steryl esters (SE), which can readily be used for lipid metabolism and energy production in response to the organism's demand (Olzmann and Carvalho, 2019; Walther et al., 2017). When the cell has an excess of fatty acids, they are converted into neutral lipids, such as TG, stored in the LDs. As energy demand increases during membrane growth, the catabolic process begins with the activation of lipolysis, which hydrolyzes the stored TG into fatty acid. Therefore, the biogenesis and breakdown of LD are tightly coupled with coordinated metabolism, and dysregulation may result in aberrant cell physiology (Welte, 2015). LD plays a critical role in preventing lipotoxicity and can buffer the amount of free toxic lipids (Olzmann and Carvalho, 2019). Furthermore, LD can also be formed inside the nucleus (Romanauska and Köhler, 2018; Sołtysik et al., 2021); therefore, its appropriate regulation is important for genomic integrity. With the recent revelation of its numerous novel functions, including host defense (Bosch et al., 2020; Monson et al., 2021) and drug delivery (Dubey et al., 2020), LD has gained enormous interest.

LD consists of a neutral lipid core surrounded by a unique phospholipid monolayer, instead of the physically coupled two-leaflets conventional bilayer membrane system (Olzmann and Carvalho, 2019). During LD budding, the phospholipid monolayer originates from the cytosolic face of the endoplasmic reticulum (ER); hence ER membrane proteins such as diacylglycerol acyltransferase (DGA2) passively move to the LD surface layer (Olzmann and Carvalho, 2019; Walther et al., 2017; Choudhary et al., 2015). In contrast, a subset of cytosolic proteins binds actively to the LD via a region anticipated to contain amphipathic helices (AHs) (Hinson et al., 2009; Barneda et al., 2015; Rowe et al., 2016; Prévost et al., 2018; Čopič et al., 2018; Chorlay et al., 2020; Du et al., 2020). The separation of hydrophobic and polar residues on two faces of a helix is the characteristic of AH. AH enriched with large hydrophobic residues exhibits a strong affinity for targeting the LD surface (Prévost et al., 2018). However, weakly associated proteins are displaced from the LD surface due to protein crowding when the LD membrane shrinks during lipolysis (Kory et al., 2015).

Pezizomycotina, the largest subphylum of Ascomycota includes research models, pathogens, and species for commercial applications (Shen et al., 2020). Pezizomycotina hyphal cells are multinucleated and exhibit a specialized multinucleated-ER bridge arrangement (data not shown; Roundtree et al., 2020). However, the biogenesis and regulation of LD in multinucleated cells/organisms are unknown. Moreover, the number of protein-encoding genes in Pezizomycotina is roughly double that of monophyletic yeast clades Saccharomycotina and Taphrinomycotina (Nguyen et al., 2017). Numerous protein families, including enzymes for plant biomass degradation and secondary metabolism, have expanded lineage-specifically in Pezizomycotina (Arvas et al., 2007), possibly via gene duplication. These gene families are either abundant in Pezizomycotina, Pezizomycotina-specific, or lacking in Saccharomycotina (Arvas et al., 2007). Furthermore, comparative genomics with global enzyme-encoding fungal genes similarly revealed an abundance of clustered candidates related to lipid metabolism in Pezizomycotina (Wisecaver et al., 2014), implying metabolic versatility and, alternatively, the emergence of energy storage machinery to counter the potential metabolic load. However, from the viewpoint of metabolic evolution, LD regulation is unknown.

Here, to identify novel LD-targeted proteins and patterns of LD regulation in Pezizomycotina, we employed a reverse genetics approach including colocalization screening with an EGFP-fused protein library. Following the functional screening, a group of novel candidates termed lipid droplet

regulating (LDR) proteins was discovered which plays an important role in LD biogenesis. LDR proteins target the LD membrane by inserting putative AHs, as demonstrated by AH-disruptive mutations and subsequent imaging. Notably, the studied AH of LdrA plays an essential role in the biogenesis of cytoplasmic and nuclear LD. Using bioinformatics, we elucidated their evolution patterns, predominantly by gene duplication.

Results

Identification of novel LD-associated proteins by colocalization screening

This study was designed with the consideration of the high metabolic potential evolved in Pezizomycotina (Arvas et al., 2007; Wisecaver et al., 2014). Therefore, to identify novel LD-targeted proteins, we employed an EGFP-fused protein library developed by our group with a set of uncharacterized proteins conserved in Pezizomycotina but absent or diverged in the representatives of Saccharomycotina and Taphrinomycotina (Fig. 1A; Mamun et al., 2022, *preprint*). A total of 314 strains (Table S1) corresponding to the organelle-like pattern of subcellular localization were analyzed here after culturing them on the minimal medium (Fig. 1A). This nutrient-limiting condition induced LD formation in *Aspergillus oryzae* (See Fig. 3A), similarly to budding yeast (van Zutphen et al., 2014). Lipophilic fluorescent dye, Nile red (Greenspan et al., 1985) was used to stain LD in the live hyphae. A total of 19 candidates were identified primarily as LD-associated after colocalization screening (Fig. 1B-D; Fig. S1A). Since the EGFP-fused protein library was developed with a large set of candidate proteins, the identified 19 candidates were further tagged with mCherry and their LD association was validated with neutral lipid dye BODIPY 493/503 (Fig. S1B, C) (Qiu et al., 2016).

Furthermore, 19 LD-associated proteins were classified as either category I or category II based on their localization patterns. Candidates classified under category I solely localized to the LD surface, but candidates under category II shared a localization with LD and other unidentified organelles (Fig. 1B-D). Twelve of the 19 proteins (including SppE and SppO) were functionally important for LD biogenesis and termed as LDR proteins (See Fig. 3). LdrA revealed two patterns of localization on LD in terms of fluorescence intensity. The population with brighter fluorescence was corresponding to nuclear LD (nLD), indicating that LdrA targets nLD more efficiently than it does cytoplasmic LD (cLD) (See Fig. S4A). Moreover, SppE and SppO, which participate in septal pore regulation (Mamun et al., 2022, *preprint*), were identified here to be associated with LD (Fig. 1C, D). Interestingly,

SppE showed a specialized LD-targeting affinity in terms of hyphal region. EGFP-labeled SppE targeted the LDs much more efficiently those residing within 100 μ m from the hyphal tip than those distributed in the basal region (Fig. 1C).

Neutral lipids are synthesized between the leaflets of the ER membrane, and their subsequent growth and maturation in the forms of LD occur towards the cytosolic side (Olzmann and Carvalho, 2019; Walther et al., 2017). Next, the subcellular localization of LD-associated proteins was evaluated by considering the distribution of the ER network. Markina-Iarriarregui et al. (2013) showed the ER network with the translocon component Sec63 in *Aspergillus nidulans*. Multiple LDR proteins and SppE exhibited accumulated localization as minute puncta on the ER membrane, which are likely the locations of early LD biogenesis (Fig. S1E). In conclusion, the current colocalization screening uncovered a group of novel candidate proteins having an association with LD.

LD-targeted proteins colocalize with nascent LD-markers Dga1 and Erg6

Diacylglycerol acyltransferase (Dga1) catalyzing the terminal step of TG biosynthesis concentrates at the subdomains of the ER membrane, which is known to be the site of early LD biogenesis (Joshi et al., 2018; Choudhary et al., 2020; Jacquier et al., 2011). Erg6, a component of the ergosterol biosynthesis pathway, is also employed as a marker of early-stage LD (Joshi et al., 2018; Choudhary et al., 2020; Jacquier et al., 2011). Several LD-associated proteins exhibited accumulated localization on the ER membrane (Fig. S1E). Next, we determined if they were associated with Dga1 and Erg6. Dga1 and Erg6 orthologues in *A. oryzae* were identified using budding yeast proteins. AoDga1 and AoErg6-EGFP colocalized predominantly with Nile red-stained LD (Fig. S2A). We analyzed the colocalization of mCherry-fused AoDga1 or AoErg6 with EGFP-labeled LDR proteins in living hyphae. Among the analyzed proteins, LdrA-LdrC, LdrG, and FccE-EGFP were largely associated with both AoErg6 and AoDga1-mCherry either as puncta or as the rim on LD (Fig. 2A–E) similar to their natural LD-localization (Fig. 1B, C). On the other hand, AoErg6-mCherry partially lost its exclusive LD-binding when co-expressed with LdrB, LdrC, and LdrI-EGFP (Fig. 2B, C; Fig. S2B, D; also See Fig. 4). Notably AoErg6-mCherry regained its natural punctate or rim-like localization when co-expressed with the less effective variants of LdrB, LdrC, and LdrI (Fig. 2B, C; Fig. S2B, D; also See Fig. 4), implying binding competition on the LD surface. However, SppF, SppI, and SppD-EGFP exhibited a dispersed localization when co-expressed with both AoDga1 and AoErg6, indicating a partial displacement from the LD membrane (Fig. S2C-E). Here, dominantly associated LdrB, LdrC, and LdrI partly expelled Erg6, whereas Erg6 partially displaced weakly associated LdrF

and LdrD from the LD surface (Fig. 2B, C; Fig. S2C-E). Remarkably, despite the observed binding competition on the LD surface, most examined proteins were predominantly associated with AoErg6 and AoDga1, frequently as tiny puncta (arrowheads in Fig. 2A-E), indicating their participation in nascent LD biogenesis.

We then examined whether LD-associated proteins physically interacted with AoErg6 using co-immunoprecipitation. The variants losing LD association (see Fig. 4; Fig. S3F) served as a negative control to differentiate false positive evaluation (Fig. S2F-I). Co-immunoprecipitation results demonstrated that neither of the analyzed proteins physically interacted with AoErg6 (Fig. S2F-I).

LDR proteins regulate LD number and size

Nineteen LD-associated proteins were identified using neutral lipid dyes (Fig. 1; Fig. S1A-D). Next, their functions on LD biogenesis were determined after the deletion of candidate gene. LD phenotypes in individual deletion were evaluated in living hyphae cultured on the minimal medium (Fig. 3A). Twelve of the 19 deletion strains exhibited aberrant LD biogenesis in terms of number and size; they have been characterized as LDR proteins (current 10 LDR proteins and two previously identified SPP proteins) (Fig. 3A-C). Ten of the functionally important candidates shared the phenotype of an increase in the average number of LDs but a decrease in their size (Fig. 3A-B), indicating defective LD growth and maturation. Whereas, *ldrC* deletion displayed the opposite characteristics, with a drop in LD number and an increase in size (Fig. 3A-C). Super-sized LD was occasionally observed in $\Delta sppE$ along with the predominant diminutive population (Fig. 3A). Notably, among the deletion mutants, *ldrA* had the most severe LD abnormalities; over twofold increases and decreases in average number and size, respectively (Fig. 3A-C). Since LdrE and LdrF as well as LdrH and LdrI were paralogues (see Fig. S5B, F), double deletions were generated for further investigation of their function. Despite the successful development of $\Delta ldrE\Delta ldrF$, we have been unable to obtain $\Delta ldrG\Delta ldrH$, even after performing multiple round transformations in alternative combinations, which suggests that $\Delta ldrG\Delta ldrH$ might have a deleterious effect on the organism. Importantly, $\Delta ldrE\Delta ldrF$ showed severe phenotypes in terms of LD number and size compared with either single deletion (Fig. 3A-C).

Expression of EGFP-fused individual gene sequence from the relevant endogenous promoter restored defective LD number and size (Fig. 3D, E) found in the corresponding deletion, demonstrating the functional relevance of the putative proteins in LD biogenesis or the validity of the EGFP constructs. Nonetheless, some EGFP-fused candidates were found on the LD surface, but others were not,

probably because of the weak EGFP signal under native expression (Fig. S1D). Finally, with functional screening, we identified LDR proteins that play an important role in LD biogenesis.

LDR proteins target LD surface via the putative amphipathic helices

During LD maturation, membrane curvature causes phospholipid (PL) packing defects (Olzmann and Carvalho, 2019). A subset of AH-containing proteins utilizes this property to directly binds from the cytosol to the LD membrane, hence promoting membrane curvature and LD growth (Bigay et al., 2012; Prévost et al., 2018; Chorlay et al., 2020). Next, we determined whether LDR proteins possess the sequence characteristic predicted to be an AH that provides binding to LD.

To predict AH, the total α -helices present in the individual LDR protein were comprehensively retrieved using Phyre2 (Kelley et al., 2015) and then analyzed with HELIQUEST (Gautier et al., 2008) which displayed the helical wheel orientation. The predicted AHs were further evaluated with AlphaFold2 (Mirdita et al., 2022) and Chimera 1.16 to show the α -helical peptide 3D model. As determined by the current systematic analysis, each LDR protein contained the AH domain (Figs. 4, 5; Fig. S3). The amphipathicity of each AH was disrupted either with truncation or point mutations and subsequently, the variants were examined for their LD-binding affinity.

A region comprising 30 residues of LdrC was predicted as AH, which shows a long hydrophobic face (Fig. 4A, Table 1). Although the AH of LdrI was comparatively short in length (20aa), its hydrophobic moment ($\langle\mu_H\rangle$) was greater than that of LdrC (Fig. 4E; Table 1). The predicted AHs in LdrC and LdrI were truncated and mutated, and the constructs were expressed in the corresponding deletion strain. In both cases, variants lacking the predicted AHs led to their complete dissociation from the LD surface (Fig. 4B, D, F, H). However, the LD binding affinity of the mutant versions of LdrC and LdrI decreased dramatically with the progressive decline of hydrophobicity in the following order: V175N/V168N/V181D<V175N/V168N>V175N>wild-type and V250N/L254D<V250N/F261N<V250N<wild-type, respectively (Fig. 4B–D, F–H; Table 1). Electrostatic interaction enhances the binding of positively charged AH to negatively charged membrane phospholipids (Čopič et al., 2018; Olarte et al., 2020). Therefore, charge swap mutants were generated by replacing positively charged residues with negatively charged ones, which negatively affected the variants' affinity to LD (Fig. 4B–D, F–H; Table 1). Furthermore, a region at the C-terminus of LdrB was predicted as AH (Fig. 4I). Truncated variant losing the predicted AH (406–437aa) resulted in a marked abolishment of its uniform rim-like

localization but showed a puncta-like attachment on the LD membrane (Fig. 4J), suggesting the presence of additional binding sites. Further analysis predicted another region (121–146aa) with a bit amphipathic nature, which was then truncated (in a variant that previously lost c-terminus AH). These truncations led to the complete elimination of LD binding affinity (Fig. 4J). The C-terminus AH was disrupted by the mutations in both hydrophobic and polar faces. LD targeting affinity markedly decreased in variants with a progressive decline of hydrophobicity and positive charge (Fig. 4J–L; Table 1).

LdrD was predicted to have a C-terminus AH (Fig. S3A). A slight decline in hydrophobicity with a single residue modulation led to the noticeable detachment of LdrD variant from both the LD surface and unrecognized cell organelle (Fig. S3B), implying weak superficial binding. LdrJ was predicted to contain an AH with a hydrophobic moment 0.44 (Fig. S3C). The variants that lacked AH or had a mutation in a critical hydrophobic residue showed dramatic disassociation from the LD surface and the unidentified cell organelle (Fig. S3D). On the other hand, two AHs with higher hydrophobic moments were predicted on LdrG (Fig. S3E). The position of the polar and hydrophobic residues was conserved in paralogue LdrH (Fig. S3E), suggesting that AHs were evolutionary conserved. The variants losing either AH revealed a minor effect, whereas that losing both showed the abolishment of the EGFP signal (Fig. S3F), implying that disassociated proteins are unstable in the cytosol. Similarly, LdrF possessed an AH that was conserved in paralogue LdrE (Fig. S3G). The variant lacking AH exhibited a similar abolishment of the EGFP signal (Fig. S3H), suggesting the instability of the unbound (to LD) protein. Taken together, our findings showed that LDR proteins bind to the LD surface via the insertion of potential AHs.

LdrA binds to and regulates LD biogenesis via a novel amphipathic helix

LdrA which is crucial for LD biogenesis contains the Opi1 domain (Fig. 5A). Budding yeast Opi1 known for the regulation of phospholipid biosynthesis revealed phylogenetic divergence from that of LdrA (see Fig. 8). Opi1 binds to phosphatidic acid (PA) through its Q2 domain and to ER membrane protein Scs2 through its FFAT motif (Loewen et al., 2004). However, the Q2 domain and FFAT motif were conserved within a limited species of *Saccharomycotina* (Fig. S4B). When inositol, a carbocyclic sugar is added to the growth media, PA levels decrease, causing Opi1 to translocate from the ER to the nucleus, where it suppresses the genes involved in phospholipid biosynthesis (Loewen et al., 2004). LdrA-EGFP, on the other hand, remained persistently localized to the LD surface in the

presence of excessive inositol (Fig. S4C). Opi1 variant lacking the Q2 domain is entirely nuclear, which results in complete repression of phospholipid biosynthesis and subsequent inositol auxotrophy (Romanauska and Köhler, 2018; Loewen et al., 2004). However, a truncated variant of LdrA, exclusively nuclear (see Fig. 5C), was not auxotrophic to inositol (Fig. S4D), implying the functional diversity of Opi1 family transcription factors.

Similar to other LDR proteins, LdrA contains a region at the C-terminus having the potential to be an AH with a hydrophobic moment of 0.34 (Fig. 5A). Importantly, the position of several hydrophobic and polar residues was conserved across the fungal representatives (Fig. 5B) implying evolutionary conservation of AH. To disrupt the putative AH, hydrophobic residues were replaced with polar asparagine (N), which maximizes the reduction of the overall hydrophobicity without altering the charge (Fig. 5C). A progressive decline in hydrophobicity from 0.39 resulted in the variants to translocate into the nucleus, visualized with the component of nuclear pore complex (NPC), Nup84 (Liu et al., 2009) (Fig. 5C-E).

In contrast, except for the AH dead mutant V420N/V416N, the variants were still associated with LD (Fig. 5C, D, F). This result can be explained by the markedly increased abundance of those mutated variants still persisting the functional AH (Fig. 5G) which were sufficient to target LD. On the other hand, replacing hydrophobic residues with similar properties (A427I and V420L) did not affect their subcellular localization to the LD membrane (Fig. 5C-F; Fig. S4E-F).

LdrA possessing net charge 0, and charge swap mutants were generated to better understand their importance in targeting the LD. Gradual enrichment of the negative charge from 0 to -4 led the variants to partial displacement from the LD to the nucleus (Fig. 5C-F; Fig. S4E, F). At the same time, the variant D422R with charge +2 did not affect the usual subcellular localization on LD (Fig. S4E-F). Taken together, our data demonstrated that the amphipathic features including hydrophobicity and positive charge played a crucial role in the binding of LdrA to the LD surface.

We then investigated if the AH has a role in LD biogenesis. LdrA variants lacking AH and AH dead mutant V420N/V416N produced many tiny LDs (Fig. 5H, I), similar to the deletion of *ldrA*. The average number of LD increased in the order of decreasing hydrophobicity A427I<V420L<M413N<C431N<V420N<V420N/V416N, but LD size followed the order of increasing hydrophobicity (Fig. 5h, I; Fig. S4G, H), demonstrating an apparent relationship between LD phenotype and hydrophobicity. Charge swap mutant R433D/K436E, on the other hand,

demonstrated an increasing LD size even above the wild type, presumably due to higher protein level or hydrophobicity (Fig. 5G–I; Fig. S4G, H). LD fusion could be one of the possible explanations reasoned for the supersized LD in variants with potential hydrophobicity, such as A427I, because LdrA-mCherry enriched at the LD–LD contact site (Fig. 5J) probably facilitates LD fusion. Taken together, the amphipathic features such as hydrophobicity and positive charge of LdrA AH played a crucial role in regulating LD biogenesis.

Furthermore, variants with impaired LD biogenesis, such as Δ AH, showed defects in asexual spore development (Fig. S4J). Whereas variants with high LD load, such as A427I, showed decreased colony development (Fig. S4J), implying a negative relationship between lipid storage and hyphal growth.

LdrA is important for the biogenesis of nuclear LD

Budding yeast Opi1 binds to and induces nLD formation after losing its association with the ER (Romanauska and Köhler, 2018). LdrA, on the other hand, usually and more efficiently targeted nLD (Fig. S4A). Next, we investigated whether LdrA is involved in the regulation of nLD biogenesis. LdrA variants were co-expressed with mCherry-labeled nuclear localizing signal (NLS) derived from transcription factor StuA (Suelmann et al., 1997). The current study eliminated apical compartments from observation which are known to be the active zone for nuclear division (Kaminskyj et al., 1998). BODIPY-positive foci that were diagnosed as nLD were often exhibited as a shadow of their shape on the nucleus (Fig. 6A). In the wild-type, approximately 7% of the nuclei bore nLD, while this ratio increased to 20% in the variant that overexpressed wildtype (native) LdrA (Fig. 6A, B). Surprisingly, 40% of nuclei were positive for nLD in M413N (Fig. 6A, B), the variant showing the highest abundance (protein content) and persisting maximum hydrophobicity among AH-disruptive mutants (Fig. 5C, G). On the other hand, the percentage of nLD dramatically decreased in the truncated variant lacking AH and AH dead mutant V420N/V416N, with a similar level observed in the deletion strain (Fig. 6A, B). However, the variants generated by replacing hydrophobic residues with similar properties (A427I and V420L) followed a similar trend to increase nLD ratio (Fig. 6AB; Fig. S4I), which collectively suggested that AH of LdrA played an important role in nLD biogenesis.

However, supersized nLD resulted in nuclear disintegration (Fig. 6A). Nup49, a component of the NPC (Liu et al., 2009), fused with mCherry, was introduced in the M413N variant to define the nuclear periphery (Fig. 6C). As expected, the nuclear periphery was disintegrated due to continuously growing supersized nLDs (Fig. 6C). Following that, we look into the degree of nuclear disruption in

M413N. NLS-mCherry which is entirely nuclear was used to visualize nuclei. The fluorescent intensity captured from the cytoplasmic pool was found greatly elevated in M413N compared to that in the wild-type control (Fig. 6D), which indicates that the leaking nucleus leads to the escape of the NLS-mCherry in the cytoplasm, and alternatively nuclear disintegration.

Next, we investigated whether LdrA nuclear import affects nLD biogenesis. To find the answer, we look for endogenous NLS using the NLS Mapper program (Kosugi et al., 2009) which projected an NLS in the middle region of LdrA (Fig. 6E). Truncated variant losing AH was exclusively nuclear (Fig. 6F). A further truncation that removed NLS resulted in the loss of predominant nuclear localization (Fig. 6F). Moreover, EGFP-NLS was adequate for nuclear signal (Fig. 6F), demonstrating that the relevant sequence is essential for nuclear import. Even though the variants lacking NLS had a slight effect on basal LD number and size, the percentage of nLD biogenesis was unaffected compared with the full-length (native) version (Fig. 6G–I), implying that a bit of nuclear import (NLS truncation did not completely eliminate nuclear import; Fig. 6F) could be sufficient to induce nLD if the variants persisting potential AH.

Binding competition regulates LD membrane composition and LD growth

Because LdrA and LdrC showed opposite phenotypes in terms of LD number and size in gene deletion and overexpression conditions (Figs. 3A–C, 5I; Fig. S1C), an extended investigation was conducted to elucidate the mode of LD regulation from them. Firstly, double deletion of the *ldrAldrC* was generated to evaluate their integrated function in LD regulation. Firstly, double deletion of the *ldrAldrC* was generated to evaluate their integrated function in LD regulation. Interestingly, double deletion of *ldrAldrC* resulted in an LD feature that partially and completely rescued the severe LD defective phenotypes found in either single deletion $\Delta ldrA$ and $\Delta ldrC$, respectively (Fig. 7A). Insertion of LdrA (overexpressed from *amyB* promoters) in $\Delta ldrC\Delta ldrA$ led to further increase in basal LD size (Fig. 7A).

Furthermore, LdrA-EGFP and LdrC-mCherry were co-expressed from heterologous *amyB* promoters to observe the colocalization patterns on the LD membrane. Co-expression resulted in the marked removal of LdrA-EGFP from the LD surface, alternatively, the LD membrane was predominantly bound by LdrC-mCherry (Fig. 7B–C). However, co-expression of LdrA with the less efficient variant of LdrC (V175N/V1678N in Fig. 4B, C) resulted in apparent improvement in the colocalization efficiency (Fig. 7B–C), which collectively suggests that LdrC had a predominant affinity to LD

membrane which might inhibit or decreased the accessibility of LdrA to the LD. Alternatively, in the absence of LdrC or decreasing its affinity, candidate proteins such as LdrA (Fig. 7C), Erg6, and Dga1 (Fig. 2B–C) could bind to the LD membrane more effectively. Collectively, LdrC can fine-tune the LD membrane composition such as LdrA and Erg6 for proper LD biogenesis.

Phylogenetic distribution and evolution of LDR proteins

We analyzed the phylogenetic distribution and the degree of divergence of LDR proteins with respect to broad data of protein sequences retrieved from representative species covering all major fungal phyla and subphyla using BLASTp (Fig. 8; Table S2A) (Ahrendt et al., 2018). Except for LdrA and LdrB, the results showed that LDR proteins evolved predominantly by gene duplication.

LdrA possessing the Opi1 domain (PF08618) (Loewen et al., 2004) showed a high degree of divergence from budding yeasts Opi1 (Fig. 8). LdrB containing transmembrane domain existed in Pezizomycotina, Mucoromycota, and a part of Basidiomycetes, but not in Saccharomycetes (Fig. 8). Notably, a total of eight LDR proteins LdrC, LdrD, LdrE, LdrF, LdrG, LdrH, LdrI, and LdrJ evolved by gene duplications. LdrC contains EI24 domain (PF07264) (Xu et al., 2022). Although basidiomycetes and several yeast species, lack orthologues, representatives from early diverging phylum possess the orthologs (Fig. 8; Fig. S5A). LdrE and LdrF contain the DUF2236 domain (PF09995). Whereas LdrG and LdrH possess the sulfotransfer-4 domain (PF17784) (Negishi et al., 2001). Notably, LdrE and LdrF as well as LdrG and LdrH are paralogues, respectively (Fig. S5B, F). Except for Saccharomycete yeasts, LdrE and LdrF dispersedly existed in the analyzed fungal phyla (Fig. 8). On the other hand, LdrG and LdrH were found abundant in early diverging Mucoromycota and Chytridiomycota; they are absent in Basidiomycetes and Saccharomycotina (Fig. 8; Fig. S5F). However, except for ascomycete yeasts, LdrJ containing the DUF829 domain (PF05705) predominantly existed in Dikarya (Fig. 8; Fig. S5G). Interestingly outgroups including humans have proteins with similar domain organizations and are possibly orthologues as assayed by reciprocal BLAST. LdrD containing DUF3659 domain (PF12396) showed scattered existence across the fungal representatives (Fig. 8). It has paralogs, indicating gene duplication (Fig. S5C). However, the subcellular localization of the paralogs was independent of LD (Fig. S5D). Interestingly, several orthologues showed N-terminal truncation. Multiple sequence alignment revealed a higher sequence homology with the C-terminal region of LdrD (Fig. S5E), implying the protein structural evolution among the fungal species. LdrI, which has an FMO-like domain (PF00743) (Lawton et al., 1994),

forms a distinct clade consisting of Pezizomycotina and Ustilaginomycotina, as well as a few species of Chytridiomycota and Taphrinomycotina (Fig. 8; Fig. S5H).

Finally, our data showed the existence of multiple proteins with almost similar domain organizations corresponding to individual LDR candidates which might have evolved by gene duplication.

Discussion

We explored the patterns of LD biogenesis in the ubiquitous fungal sub-phylum Pezizomycotina, which has high metabolic potential but has not yet been thoroughly analyzed. Using reverse genetics, we identified a subset of poorly characterized proteins (LDR proteins) that play a potential role in LD biogenesis. LDR proteins possess a specific sequence motif, AH, that mediates the binding of candidate proteins to the LD surface. Candidates having AH with a large superficial hydrophobicity had a binding advantage over their counterparts, influencing LD dynamics. Our study suggested gene duplication is as the mechanism for the evolution of LDR proteins in Pezizomycotina

Known LD-associated components are either identified with forward genetics or biochemical strategy (Guo et al., 2008; Szymanski et al., 2007; Fei et al., 2008; Currie et al., 2014; Pataki et al., 2018). However, forward genetics screening is often laborious due to genome-wide manipulation (Guo et al., 2008; Szymanski et al., 2007). Here, we applied a reverse genetics strategy for the first time by utilizing the previously established EGFP-fused protein library (Mamun et al., 2022 *preprint*). Colocalization analysis with LD staining dyes Nile red and BODIPY, and subsequent cross-checking with LD maker proteins Erg6 and Dga1, provided high confidence in our primary data set consisting of 19 candidate proteins (Figs. 1, 2; Fig. S1). Multiple LDR proteins localized as minute puncta-like structures on the ER membrane (Fig. S1E), leaving unanswered questions for future research, such as whether and/or how they are involved in lipid synthesis or nascent LD biogenesis.

Nearly two-thirds of LD-associated proteins had functional importance in LD biogenesis (Fig. 3A-C). The reverse correlation between LD number and size observed in the individual deletion (Fig. 3A, B) suggested a defect in LD growth and maturation. However, lipid profiling remains to be performed in the individual deletion strain to evaluate any alternation in lipid contents. Furthermore, reduced colony development observed in aberrant-LD-producing strains (Fig. S4J) may have been caused by an inadequacy of free phospholipids for membrane proliferation due to excessive storage. As lipid

homeostasis is crucial for growth, numerous fungicides, including azole, target it (Revie et al., 2018). CCG-8 and UsgS, the orthologues of LdrA and LdrC in *Neurospora crassa* and *Aspergillus fumigatus*, respectively are upregulated in response to azole drugs (Sun et al., 2018; da Silva et al., 2006), which provides a hypothesis that LD confers host adaptation to the antifungal drug.

LD membrane proteome includes both anabolic and catabolic components such as lipid synthesizing enzymes and lipase, respectively, and therefore plays a crucial role in LD turnover (Olzmann and Carvalho, 2019; Walther et al., 2017). Candidate protein's accessibility to the LD surface is found to be constrained by either barrier development surrounding the LD (Brasaemle et al., 2000) or by protein crowding alternatively binding competition (Kory et al., 2015; Wang et al., 2006; Listenberger et al., 2007). The monolayer membrane bears a relatively large phospholipid packing defect than that of the bilayer (Prévost et al., 2018). Proteins with affinity (to LD) directly bind from cytosol to LD surface which crowd the phospholipids and subsequently reduce LD surface hydrophobicity. This biochemical alteration may expel weakly-associated proteins or limit their capacity to further bind. For example, adipocyte differentiation-related protein (ADRP) demonstrates predominant affinity to the LD surface over adipose triglyceride lipase (ATGL), modulating LD dynamics (Listenberger et al., 2007). Similarly, the predominant binding of LdrC resulted in a fine-tuned association of LdrA to the LD surface (Fig. 7B-C), which may play a major role in the biogenesis of proper size-LD, because LdrA facilitated LD fusion (Fig. 5J).

The LD surface is promiscuous for interacting with AH-carrying proteins, and the binding performance is heavily influenced by amphipathic properties such as hydrophobicity, hydrophobic moment (Eisenberg et al., 1982), and charge (Prévost et al., 2018; Čopič et al., 2018; Pataki et al., 2018). Among them, axial hydrophobicity of the candidates is crucial for stable association with LD membrane (Prévost et al., 2018; Pataki et al., 2018; Čopič et al., 2018). AH-possessing DHRS3 with a larger axial hydrophobic surface is suggested to stably bind to LD using broad interactions with phospholipid acyl chains (Pataki et al., 2018). Here, LdrB, LdrC, and LdrI contained AH with a large hydrophobic surface that conferred strong LD-binding affinity to partially expel Erg6 from the LD surface (Fig. 2B, C; Fig. S2D). On the other hand, phosphocholine cytidyltransferase1 (CCT1) AH enriched with charged residues, binds weakly and thus can fall off from the LD surface during lipolysis (Kory et al., 2015; Taneva et al., 2012). In the present study, LdrA and LdrF comparatively enriched with polar residues were expelled from LD when co-expressed with LdrC and Erg6,

respectively (Fig 7A; Fig. S2C). However, unbound (due to removal of AH) forms of LdrD, LdrE, LdrG, and LdrJ were unstable in the cytosol with a similar phenomenon reported for ubiquitous mammalian LD protein, Perilipins (Rowe et al., 2016), implying that their abundance and stability could be increased under high LD load. Many AHs are reported to remain disordered in the aqueous environment and transiently folded into helical confirmation in the interface between the hydrophobic LD and the hydrophilic cytosol (Čopič et al., 2018; Hofbauer et al., 2018). Since it has been postulated that most of the LDR proteins bind to the LD from the cytosol (Fig. 1, category I), it remains to be determined if these are still folded in the cytosol or would be folded at the cytosol-LD interface.

Although a metabolic switch regulated by Opi1 plays an important role in LD biogenesis in budding yeast (Romanauska and Köhler, 2018), our findings demonstrated the structural basis of LD regulation by a novel AH found on LdrA. Opi1 shows functional divergence even among yeast orthologues, such as alkane oxidation in *Yarrowia lipolytica* (Hirakawa et al., 2009) and filamentous growth in *Candida albicans* (Chen et al., 2015). Opi1 binds to the Ino2 via its activator interaction domain (AID) domain and subsequently represses genes involved in phospholipid biosynthesis (Heyken et al., 2005). The sequence similarity of Ino2 is limited within a portion of saccharomycotina (data not shown), implying that phospholipid biosynthesis is regulated differently in Pezizomycotina. However, whether LdrA transcriptional activity (if exist any) is involved in LD biogenesis in Pezizomycotins remains to be investigated. The cellular LdrA level is fine-tuned to regulate proper LD dynamics in native condition. The rate-limiting LdrA level (native in Fig. 5G) may be owing to a bottleneck in protein folding, as previously described in Rop, a dimeric four-helix-bundle protein, where mutations at the hydrophobic core markedly increase protein content (Munson et al., 1997) similarly to M413N variants of LdrA (Fig. 5G). However, the controlled LdrA level is beneficial for fungal growth, since LdrA induced lipid storage with the biogenesis of supersized LD (Fig. 5I). LdrA induced the formation of both supersized cLD and nLD (Figs. 5, 6). Supersized nLD could have a greater impact on uninucleate cells like budding yeast, which could be mitigated by limiting the nuclear import of Opi1 by primary binding with ER (Loewen et al., 2004). Alternatively, the lethal effect resulting from the nuclear degradation due to supersized nLD (Fig. 6AB) might be compensated with the multinucleate nature of *A. oryzae* in which even if some of the nuclei are disintegrated the remaining can support its survival. LdrA bound to both nLD and cLD (Fig. S4A). The high-affinity binding of LdrA to nLD (Fig. S4A) is possibly due to the absence of competitors

inside the nucleus, since this organelle allows only those proteins containing NLS to enter, therefore LdrA can freely target nLD.

Our phylogenetic analysis revealed that LDR proteins existed preferentially in Pezizomycotina and several lineages of Mucoromycota and Basidiomycota but are mostly absent or diverged in monophyletic Saccharomycotina (Fig. 8; Fig. S5A-H). Yeasts undergo progressive gene loss after whole genome duplication (Kiss et al., 2019), but have evolved a specialized metabolism, known as fermentation (Novo et al., 2009; Pronk et al., 1996). Fermentation is a catabolic process that converts sugars into ethanol. Since yeast is less efficient in storing energy due to its fermentative metabolism, LDR proteins evolved early in fungal evolution could be lost, due to the selection pressure as irrelevant to cell physiology. On the other hand, with few exceptions, LDR proteins showed considerable existence in the several lineages of Mucoromycota (Fig. 8; Fig. S5A–H). Supporting the observed abundance, several Mucoromycota lineages possess a remarkable potency to accumulate intracellular lipids ranging from 20 to 80% (w/w) and form lipid bodies up to 20 μm in size (Kosa et al., 2018; Dzurendova et al., 2022). Importantly, LDR proteins predominantly existed in all the major classes of Pezizomycotina and showed a tendency for gene duplication, implying a parallel evolution along with the reported Pezizomycotina-specific metabolism-related genes (Arvas et al., 2007; Wisecaver et al., 2014). Thus, we hypothesized that the requirement of energy storage for the adaptation to nutrient depletion in saprophytes and parasites (Naranjo-Ortiz et al., 2019) and lineage-specific metabolic potency (Arvas et al., 2007; Wisecaver et al., 2014) could be the driving force for the evolution of LDR proteins by gene duplication to support lipid storage for maintaining the energy balance.

Here, reverse genetics was employed for the first time to discover the LDR proteins which is expected to create a breakthrough in the identification of novel LD-regulating proteins. Our study provides substantial molecular insight into the LD-targeting mechanism by AH-anchoring proteins and its significance in LD biogenesis. Furthermore, several LDR proteins possess known domains including predicted enzymes, and domains those functions have yet to be determined. This study provides a platform for future investigation to elucidate the specific function of individual LDR proteins in lipid metabolism.

Materials and methods

Strains, media, growth conditions, and fungal transformation

The strains employed in this work are listed in Table S3. Transformation of *A. oryzae* was performed as previously described (Maruyama and Kitamoto, 2011). *Aspergillus oryzae* strain NSPID1 (*niaD*⁻ *sC*⁻ Δ *pyrG* Δ *ligD*) (Mamun et al., 2020) was used as the parent strain. Transformants containing the *pyrG* selectable marker were selected using M+Met medium (0.2% NH₄Cl, 0.1% (NH₄)₂SO₄, 0.05% KCl, 0.05% NaCl, 0.1% KH₂PO₄, 0.05% MgSO₄·7H₂O, 0.002% FeSO₄·7H₂O, 0.15% methionine, and 2% glucose; pH 5.5). Transformants with the *niaD* and *sC* selectable markers were selected using CD medium (0.3% NaNO₃, 0.2% KCl, 0.1% KH₂PO₄, 0.05% MgSO₄·7H₂O, 0.002% FeSO₄·7H₂O and 2% glucose; pH 5.5) and CD+Met medium supplemented with 0.0015% methionine, respectively. *A. oryzae* strains were maintained at 30°C on PD plate (Nissui, Tokyo, Japan). For transformation, strains were inoculated into DPY liquid medium (0.5% yeast extract, 1% hipolypeptone, 2% dextrin, 0.5% KH₂PO₄, 0.05% MgSO₄·7H₂O, pH 5.5) and cultured overnight with constant shaking. For microscopy, conidia were inoculated on glass-based dishes containing CD or M medium supplemented with 1% casamino acids.

Plasmid construction and strain development

Construction of strains expressing mCherry-tagged 19 LD-associated proteins

The open reading frames of 19 LD-associated proteins were amplified from RIB40 genomic DNA with PrimeSTAR[®] HS DNA Polymerase (TaKaRa, Otsu, Japan) for high-fidelity PCR, using primers listed in Table S4. The amplified fragments were then fused with *Sma*I-linearized *pisCIIA*-mCherry (Mamun et al., 2020) using the In-Fusion HD Cloning Kit (TaKaRa Bio, Otsu, Japan). Recombinant plasmids for the expression of mCherry-fused 19 proteins were digested with *Not*I and ectopically inserted into the *sC* locus of the wild-type strain NSID1 (Mamun et al., 2020) by homologous recombination (Fig. S1B, C).

Construction of strains expressing mCherry-tagged Aoerg6 and AoDga1 for colocalization with EGFP-tagged LDR proteins

For colocalization analysis (Fig. 2; Fig. S1E, 2A-E), *A. oryzae* proteins AO090026000845, AO090011000289, and AO090005001238 were identified as orthologues Dga1, Erg6, and Sec63, respectively in budding yeast proteins. The open reading frame (ORF) of three respective genes were

amplified from RIB40 genomic DNA using primers listed in Table S4. The amplified fragments were then fused with *Sma*I-linearized *pisCIIA*-mCherry (Mamun et al., 2020). Recombinant plasmids for the expression of mCherry-fused proteins were digested with *Not*I and ectopically inserted into the *sC* locus of the NSID1. The resultant strains expressing AoDga1-mCherry and AoErg6-mCherry were further transformed (ectopically) with *Not*I digested EGFP-fused plasmids (Mamun et al., 2022, *preprint*) corresponding to analyzed LD-associated proteins and newly developed EGFP-tagged less efficient variants (see later) of LdrB, LdrC and LdrI into the *niaD* locus by homologous recombination. Strain expressing AoSec63-mCherry was ectopically transformed with 12 EGFP-fused LD-associated proteins (Fig. S1E).

Construction of HA- and FLAG-tagged strains for co-immunoprecipitation analysis

For co-immunoprecipitation analysis (Fig. S2F–I), full-length sequences of LdrA, LdrB, LdrC, and LdrG were amplified from the RIB40 genomic DNA using the primers listed in Supplementary Data 4. The constructs abolished for LD binding affinities such as LdrA (Δ AH Δ NLS), LdrB (Δ AH Δ 121-146), LdrC (V175N/V168N/V189N), and LdrG (Δ AH1 Δ AH2) were amplified from already developed *pUtNAldrA*(Δ AH Δ NLS)N-EGFP, *psiCII-ldrB*(Δ AH Δ 121-146)A-mCherry, *psiCII-ldrC*(V175N/V168N/V189N)A-mCherry, and *psiCII-ldrG*(Δ AH1 Δ AH2)A-EGFP, respectively (see later). The amplified DNA fragments were then fused with *Sma*I-digested linearized *pUtNAhaN*, provided by Dr. Takuya Katayama (Department of Biotechnology, The University of Tokyo, Japan). The *Not*I-digested recombinant plasmids were then inserted into the *NiaD* locus of the corresponding deletion strains. The ORF of AoErg6 was amplified from already developed *psiCII-erg6A*-mCherry, and the fragment was fused with *Sma*I-digested linearized *pisCA-FLAG* provided by Dr. Takuya Katayama (Department of Biotechnology, The University of Tokyo, Japan), yielding *pisCerg6A-FLAG*. The *Not*I-digested *pisCerg6A-FLAG* were ectopically inserted into the *sC* locus of all the HA-expressing strains mention above.

Generating LDR gene deletions library

Primers used for the generation of the deletion strains (Fig. 3A-C) are listed in Table S4. Replacement of individual genes with the Orotidine-5'-phosphate decarboxylase (*pyrG*) marker was performed by amplifying 1.5 kb upstream and 1.5 kb downstream of the gene of interest using the primer sets *gene-upstream1_F/gene-upstream2_R* and *gene-downstream1_F/gene-downstream2_R*, respectively. The

pyrG marker was amplified from RIB40 genomic DNA using the primers PyrG_F and PyrG_R. The three amplified DNA fragments (upstream, and downstream regions of targeted genes and *pyrG*) and linearized-pUC19 vector were fused using the In-Fusion HD Cloning Kit. Deletion constructs were further amplified using the primer set gene-upstream1_F/gene-downstream2_R from the resultant plasmid, and then introduced into the native locus of the *A. oryzae* strain NSPID1 (Mamun et al., 2020) by homologous recombination. Transformants were selected using uridine/uracil prototrophy.

Generating double deletion strains

To generate double deletions (Fig. 3A, B; 7C), 1.5 kb upstream and 1.5 kb downstream of *ldrF*, *ldrH*, and *ldrA*, were amplified from RIB40 genomic DNA using the primer sets gene-upstream1_F/gene-upstream2_R and gene-downstream1_F/gene-downstream2_R, respectively listed in Table S4. The ATP sulfurylase (*sC*) marker was amplified separately. The three amplified DNA fragments (upstream, and downstream regions of targeted genes and *sC*) and linearized-pUC19 vector were fused. Deletion constructs were further amplified using the primer set gene-upstream1_F/gene-downstream2_R from the resultant plasmid. PCR-amplified deletion constructs of *ldrF*, *ldrH*, and *ldrA* were introduced into the native loci of $\Delta ldrE$, $\Delta ldrG$, and $\Delta ldrC$, respectively.

Expression of EGFP-tagged LDR and SPP proteins from the endogenous promoter

For complementation of the deletions (Fig. 3D, E), the DNA fragments from 1.4 kb upstream until the stop codon and 0.6 kb downstream of the respective genes were amplified separately from RIB40 genomic DNA using primers listed in Table S4. EGFP sequence was amplified from pUt-EGFP (Mamun et al., 2020) using EGFP_F and EGFP_R. The amplified three fragments (upstream + ORF, downstream, and EGFP) were fused with a *Sma*I-linearized pUXN (Mamun et al., 2020) vector, yielding pUgeneN-EGFP. The resultant recombinant plasmids were digested with *Not*I and introduced into the *niaD* locus of the corresponding deletion strain by homologous recombination. For negative control, the individual deletion strain was introduced with *Not*I-digested PUXN vector into the *niaD* locus.

Construction of truncations and AH-disrupting mutants of LDR proteins

To truncate the putative AH (LdrC, LdrI, and LdrB in Fig. 4; and LdrA in Fig. 5) as well as LdrG and LdrF in (Fig. S3F, H), the flanking ORF fragments before and after AH were separately amplified from corresponding EGFP-fused plasmids bearing full-length sequence. When putative AH was

located at the extreme C-terminus (LdrD and LdrJ in Fig. S3B, D), the fragments from the start codon until AH were amplified. To construct AH disrupting mutants (Figs. 4, 5C; Fig. S3B, D), the customized primers containing 15 bp overlapping sequence, which bear the desired mutations were used to amplify the flanking ORF fragment before and after the targeted sites. To develop double (such as V175N/V168N in Fig. 4B) or triple mutants (such as V175N/V168N/V189D in Fig. 4B), flanking ORF fragments before and after the targeted sites were amplified from the corresponding formerly developed single or double mutations bearing plasmids. When putative AH was located at the end of C-terminus such as LdrA, LdrD, and LdrJ (Fig. 5C; Fig. S3B, D), the flanking ORF fragments after the targeted sites were amplified till the terminator of *amyB* (*TamyB*). Three fragments including upstream flanking, downstream flanking, and *SmaI*-linearized either pUt-EGFP (LdrA variants in Fig. 5C; LdrJ, LdrG, and LdrF in Fig. S3D, F, G) or pisCIIA-mCherry (LdrC, LdrI, and LdrB variants in Fig. 4; LdrD in Fig. S3B) were fused. The resultant plasmids were digested with *NotI* and then introduced either into the *niaD* (LdrA, LdrJ, LdrF, and LdrG) or *sC* (LdrC, LdrI, LdrB, and LdrD) locus of the corresponding deletion strain by homologous recombination. At the same time plasmids corresponding to wild-type sequences tagged either with EGFP or mCherry were also inserted into the respective deletion background for later used as the positive control.

Expression of NLS (AoStuA)-, AoNup84-, and AoNup49-mCherry

To visualize nuclear periphery (Figs. 5D, 5F, 6C), components of NPC Nup84 and Nup49 were used. *Aspergillus oryzae* proteins AO090138000215 and AO090023000199 were identified as the orthologues of *Aspergillus nidulans* corresponding proteins. The ORF of AoNup84 and AoNup49 were amplified from RIB40 genomic DNA using primers listed in Table S4. Similarly, to visualize the nucleus (Fig. 6A, B), the C-terminal region, referred to as NLS (400–645aa, which contains NLS located outside of the functional domain) of StuA was amplified from RIB40 genomic DNA. All the fragments including AoNup84, AoNup49, and StuA (NLS) were then fused individually with *SmaI*-linearized pisCIIA-mCherry. Recombinant plasmids were digested with *NotI* and ectopically inserted into the *sC* locus of the $\Delta ldrA$ and wild-type NSID1. Already developed plasmids (above mentioned) containing EGFP-fused LdrA variants were digested with *NotI* and then introduced either into the *niaD* of $\Delta ldrA$ expressing AoNup84-mCherry (Figs. 5D, 5F; 6C). Here, for the development of the untagged version (Figs. 5H, 5I, 6AB), the DNA fragment of LdrA variants including truncated, mutated, and wild-type were amplified until the stop codon from the above developed (Fig. 5C) EGFP-fused respective plasmids, and subsequently fused with *SmaI* linearized pUtNAN (Mamun et

al., 2020). To construct LdrA variants expressed from the endogenous promoter, the fragments 1.4 kb upstream and those from the start codon till *TamyB* were separately amplified from RIB40 genomic DNA and the corresponding plasmids (mentioned above as: untagged version), respectively. The two amplified fragments (upstream and ORF) were fused with the *SmaI*-linearized pUXN vector. Resultant plasmids bearing LdrA variants expressed either from the heterologous or endogenous promoter were digested with *NotI* and then introduced into the *niaD* locus of $\Delta ldrA$ expressing NLS (StuA)-mCherry (Figs. 5H, 5I, 6A, 6B) and AoNup49-mCherry (M413N in Fig. 6C).

Truncation, as well as expression of EGFP-tagged NLS(LdrA)

To construct the truncated variant lacking the predicted NLS in LdrA (Fig. 6F), flanking ORF fragments before (1–188aa) and after (225–482aa) of NLS region were amplified from plasmids pUtNAldrA(Δ AH)N and pUtNAldrAN using primers listed in Supplementary data 4. The amplified fragments separately were fused with pUt-EGFP yielding pUtNAldrA(Δ AH Δ NLS)N-EGFP and pUtNAldrA(Δ NLS)-EGFP. Similarly, the NLS fragment (189–224aa) was amplified from RIB40 genomic DNA and subsequently fused with EGFP-pUt (Mamun et al., 2020) resulting in EGFP-pUtNAldrA(Δ NLS). Resultant plasmids were digested with *NotI* and introduced into the *niaD* of $\Delta ldrA$ expressing AoNup84-mCherry (Fig. 6F). The full-length and fragments lacking the NLS were amplified from pUtNAldrAN and pUtNAldrA(Δ NLS)-EGFP, respectively. The fragments were fused individually with HA-pUtNAN provided by Dr. Takuya Katayama (Department of Biotechnology, The University of Tokyo, Japan). Extracted plasmids were digested with *NotI* and introduced into the *niaD* of $\Delta ldrA$ expressing NLS (StuA)-mCherry (Fig. 6G-I).

Co-expression of LdrA-EGFP and LdrC-mCherry, as well as overexpression of LdrA in AldrA AldrC

For co-expression (Fig. 7B-C), a full-length LdrA fragment was amplified from RIB40 genomic DNA using primers listed in Table S4. The amplified fragment was then inserted into the *SmaI* site of pUtNAN (Mamun et al., 2020), yielding pUtNAldrAN. The subsequent plasmid and already developed pUtlDrA-EGFP were digested with *NotI* and ectopically introduced into the *niaD* locus of NID1-LdrCmChry and NID1-LdrC(V175N/V168N)mChry (mentioned above). For complementation (Fig. 7A), *NotI* digested pUtNAldrAN was introduced into the *niaD* of double deletion *ldrAldrC* using homologous recombination.

Fluorescent microscopy and image processing

Living hyphae expressing EGFP and mCherry-tagged proteins or staining with LD dye BODIPY and Nile red were observed using an IX71 inverted frame confocal microscope (Olympus, Tokyo, Japan) equipped with 100× Neofluar objective lenses (1.40 numerical aperture); 488- (Furukawa Electric, Tokyo, Japan) (BODIPY, EGFP) and 561-nm (Melles Griot, Rochester, NY, USA) (Nile red, mCherry) semiconductor lasers, GFP filters (Nippon Roper, Tokyo, Japan); a CSU22 confocal scanning system (Yokogawa Electronics, Tokyo, Japan), and an Andor iXon cooled digital CCD camera (Andor Technology PLC, Belfast, UK). Images were analyzed using Andor iQ 1.9 software (Andor Technology PLC), and exported to TIFF files.

To analyze the percentage of AoErg6-mCherry and AoDga1-mCherry colocalized with EGFP-fused LDR proteins, the total mCherry-positive (population 1) or EGFP-positive (population 2) area regardless of the particular distribution pattern was calculated using the color threshold tool in ImageJ version 15.3 (Schneider et al., 2012). The area corresponding to the colocalized intersection between EGFP and mCherry channels was calculated by adjusting a similar set of the color threshold tool (population 3). Quantification settings were identical within a single experiment. The Percentage of colocalization for mCherry channel was calculated using the following formula (Rowe et al., 2016): $\text{Population 3} / \text{Population 1} \times 100$ (Rowe et al., 2016). The Percentage of colocalization for EGFP channel was calculated using the following formula: $\text{Population 3} / \text{Population 2} \times 100$.

The colocalizations of BODIPY- (Figs. 4D, 4H, 4L, 7B; Fig. S3B) or Nile red-stained (Fig. 5E; Fig. S3D, S3F) LD with mCherry- or EGFP-tagged LDR proteins, respectively were analyzed using FIJI. The total number of LDs and the LD colocalized with LDR proteins were counted using the particle detection tools of Plugins of FIJI. The colocalization percentage was calculated from colocalized-LD divided by the total number of LD and multiplied by 100 (Colocalization percentage = colocalized-LD/ total LD X 100).

Similarly, the nLD number (Fig. 6B, 6G) was counted using the colocalization of NLS-mCherry positive with BODIPY-stained nLD from the hyphal area except for the apical compartment. The total number of nuclei was then counted with the specified area and the value was presented as a percentage (Fig. 6B, 6G).

To quantify fluorescent intensity, the images from EGFP or mCherry-fused LDR variants were captured during a single session at identical excitation and detection settings from live hyphae. Fluorescent intensity was measured by drawing the single transverse line on the LD membrane (Figs. 1C, 4C, G, K, 5D) or nucleus (Fig. 5D) or hyphae (Fig. 6D) using the plot profile tool in ImageJ

(Schneider et al., 2012). The grey value corresponding to each pixel was taken and represented as average intensity.

LD staining and quantification

Strains were cultured on the liquid minimal medium in glass bottom dish for 20 h, and the medium was replaced with fresh medium containing either 0.5 µg/ml BODYPY 493/503 or 10 µg/mL Nile red (Sigma, St. Louis, Missouri, USA). The culture containing the staining solution was incubated for 10 min at room temperature. Due to the filamentous shape of fungal hyphae, the hyphal areas covering one window size (×100 lens) equivalent to 45 µm were captured preferentially from a uniform and non-clustered LD region with identical microscopy conditions. Fluorescent Images were taken with ×100 objective lens and captured with an 8-bit setting and subsequently stored in the tiff file format. The images captured from at least three independent experiments were analyzed using ImageJ software. LD number and size within the analyzed were quantified using the “analyze particles” tool in ImageJ with size (pixel²) settings from 0.1 to 1000 and circularity from 0 to 1. Identical thresholds were applied to all experimental conditions. The values were presented as average.

Western blotting and co-immunoprecipitation

Strains were cultured on minimum medium (CD liquid medium) for 20 h to induce LD biogenesis. The fungal mycelium was harvested in liquid nitrogen and subsequently grinded with multi bead shocker. After extracting, cell lysates were incubated with the buffer containing detergent NP-40 (50 mM Tris-HCl (pH 8.0), 200 mM NaCl, 1 mM/ mL PMSF, 1 mM/ mL Protease inhibitor, 1% NP-40) to solubilize the membrane protein. Mycelial extract solubilized with the buffer was incubated in ice for 20 min. After centrifugation with 1000x g for 10 min, the supernatant was collected. The protein samples were separated using 10% SDS-PAGE, and then transferred to Immobilon-P polyvinylidene difluoride (PVDF) membranes (Millipore, Bedford, MA, USA) using a semidry blotting system (Nihon Eido, Tokyo, Japan). To detect EGFP, Living Colors[®] A.V. monoclonal antibody (cat # 632380, 1: 2,000, Clontech) and horseradish peroxidase (HRP)-labeled anti-mouse IgG (H + L) (cat #, 7076S, 1: 2,000, Cell Signaling Technology, Danvers, MA, USA) were used as primary and secondary antibodies, respectively (Fig. 5G). For co-immunoprecipitation, cell lysates were incubated with Anti-HA magnetic Agarose (cat # M-180-10, MBL Co., Ltd, Nagano, Japan) for 3 h in 4°C at axial rotation. The purified proteins were separated with SDS-PAGE, and transferred to PVDF membranes. For detection of HA, Anti HA-tag monoclonal antibody (cat # M180-3, 1:2000, MBL

Co., Ltd, Nagano, Japan) and HRP-linked anti-mouse IgG (cat #, 7076S, 1: 2,000, Cell Signaling Technology, Danvers, MA, USA) were used as primary and secondary antibodies, respectively. To detect ELAG, anti-DDDDK-tag polyclonal antibody (cat # PM020, 1:2,000, MBL Co., Ltd, Nagano, Japan) and HRP-linked anti-rabbit IgG (cat # 7074P2, 1:2,000, Cell Signaling Technology, Danvers, MA, USA) were used as primary and secondary antibodies, respectively. Chemiluminescence was detected using a Western Lightning-ECL system (PerkinElmer, Waltham, MA, USA) and an LAS-4000 image analyzer (GE Healthcare, Buckinghamshire, UK).

Prediction of Amphipathic helices

To predict the AH, all the LDR proteins were comprehensively analyzed with Phyre2, a protein fold recognition server (Kelley et al., 2015) to retrieve the α -helix region. Each α -helix was then analyzed with HELIQUEST (Gautier et al., 2008) to know the helical wheel orientation. If the helical wheel showed segregation of helix into the hydrophobic face with considerable length and polar face especially enriched with positively charged, then these are considered. The α -helix with hydrophobicity ($\langle H \rangle$) and hydrophobic moment ($\langle \mu H \rangle$) above 0.30 were set as the criteria to be taken (Čopić et al., 2018). The predicted AH was further analyzed with AlphaFold2 (Mirdita et al., 2022) and Chimera 1.16 to evaluate the distribution of hydrophobic and polar residues in the helix.

Phylogenetic analysis

LDR proteins were investigated using Simple Modular Architecture Research Tools (SMART: <http://smart.embl-heidelberg.de/>) (Schultz et al., 1998) to identify predicted domains. The domain organizations were further cross-checked with NCBI and InterPro site. Multiple sequence alignments were performed to analyze sequence conservation using ClustalW (Thompson et al., 2002).

We followed a previously described for analyzing substitution rate (Fig. 8) of each LDR protein from Pezizomycotina root (Nguyen et al., 2017). Briefly, we performed BLASTp ($\leq 1.0e-5$) to search and retrieve the best hit protein from representative fungal species (Supplementary Data 2A) using individual LDR proteins as the query. Multiple sequence alignments were built for individual proteins using ClustalW (Thompson et al., 2002) with default setting of gap penalties. Maximum likelihood trees were generated for each LDR protein using PhyML. Phylogenetic trees were crosschecked by further constructing them with molecular evolutionary genetics analysis (MEGA) tool (Kumar et al., 2016). The substitution rate was calculated for an individual species x in the corresponding tree, the

evolutionary distance between protein sequences and Pezizomycotina ancestral sequences of *A.*

oryzae LDR proteins was estimated by the score: $s(x) = d(x) - \frac{\sum_{y \in \text{Pezizomycotina}} d(y)}{P}$

(Unit: substitutions/site),

where $d(x)$ indicates the branch length from species x to the Pezizomycotina root. The variable $d(y)$ represents the branch length from species y (in Pezizomycotina) to the Pezizomycotina root and P represents the number of species in Pezizomycotina y used in phylogenetic analysis.

Reciprocal BLAST (Hernández-Salmerón et al., 2020; Li et al., 2003; Ward et al., 2014) was used to find orthologues in *A. oryzae* (Table S2B) with the best hit candidates (Table S2A, used in substitution rate analysis in Fig. 8) as the query. To elucidate the pattern of gene evolution, additional phylogenies were generated using fungal proteins with shared domains (Fig. S5). All proteins within a given species containing analyzed domains were retrieved from the FungiDB genome database. Domain information for those species not covered by the FungiDB database was retrieved from UniProt. Phylogenetic trees for analyzed proteins were constructed using Mega X (Kumar et al., 2016).

Statistical analysis

The results of at least three independent experiments are presented as means. Error bars represent standard deviations as indicated in the figure legends. Statistical significance was tested with the two-tailed Student's t -test using Microsoft Excel; significance is indicated as ns-not significant $p > 0.05$, $*p < 0.05$, $**p < 0.01$, $***p < 0.001$, $****p < 0.0001$

Acknowledgments

We are highly grateful to Professor Jun-Ichi Maruyama, Brewing Microbiology Lab, The University of Tokyo, Japan, for laboratory support, including ensuring availability of all the reagents and instruments used in this study from his own research fund allocated in Brewing Microbiology Lab. He also provided helpful advice in this study. We are also grateful to Dr. Shinichi Nishimura Microbiology Lab, The University of Tokyo for providing BODIPY 493/503 and related suggestions for the study. We are also thankful to Dr. Takuya Katayama from Brewing Microbiology Lab, The University of Tokyo for providing the parent plasmids used in the CO-IP experiment.

Author contributions

M. A. A. Mamun conceived of and designed the study. M. A. A. Mamun performed all the experiments and bioinformatics analysis. M. A. A. Mamun and M. A. Reza interpreted the results. M. A. Reza and M. S. Islam provided relevant scientific advice to conduct the study. M. A. A. Mamun wrote the manuscript. All authors have read and approved the final manuscript.

Competing interests

The authors declare no competing interests

Data availability

All data supporting the findings of the present study are available in this article and Supplementary Information files, or from the corresponding authors upon request.

Abbreviations

lipid droplets; LD

lipid droplet regulating; LDR

amphipathic helices; AH

nuclear localizing signal; NLS

horseradish peroxidase; HRP

References

- Ahrendt, S. R., Quandt, C. A., Ciobanu, D., Clum, A., Salamov, A., Andreopoulos, B., Cheng, J. F., Woyke, T., Pelin, A., Henrissat, B., Reynolds, N. K., Benny, G. L., Smith, M. E., James, T. Y., Grigoriev, I. V. 2018. Leveraging single-cell genomics to expand the fungal tree of life. *Nat. Microbiol.* 3:1417-1428.
- Arvas, M., Kivioja, T., Mitchell, A., Saloheimo, M., Ussery, D., Penttila, M., Oliver, S. 2007. Comparison of protein coding gene contents of the fungal phyla Pezizomycotina and Saccharomycotina. *BMC Genomics.* 8: 325.
- Barneda, D., Planas-Iglesias, J., Gaspar, M. L., Mohammadyani, D., Prasannan, S., Dormann, D, Han, G. S., Jesch, S. A., Carman, G. M., Kagan, V., Parker, M. G., Ktistakis, N. T., Klein-Seetharaman, J., Dixon, A. M., Henry, S. A., Christian, M. 2015. The brown adipocyte protein CIDEA promotes lipid droplet fusion via a phosphatidic acid-binding amphipathic helix. *Elife.* 4: e07485.
- Bigay, J., Antony, B. 2012. Curvature, lipid packing, and electrostatics of membrane organelles: defining cellular territories in determining specificity. *Dev. Cell.* 23: 886-895.
- Bosch, M., Sánchez-Álvarez, M., Fajardo, A., Kapetanovic, R., Steiner, B., Dutra, F., Moreira, L., López, J. A., Campo, R., *et. al.* 2020. Mammalian lipid droplets are innate immune hubs integrating cell metabolism and host defense. *Science.* 370: eaay8085.
- Brasaemle, D. L., Rubin, B., Harten, I. A., Gruia-Gray, J., Kimmel, A. R., Londos, C. 2000, Perilipin A increases triacylglycerol storage by decreasing the rate of triacylglycerol hydrolysis. *J. Biol. Chem.* 275: 38486-38493.
- Chen, Y. L., de Bernardis, F., Yu, S. J., Sandini, S., Kauffman, S., Tams, R. N., Bethea, E., Reynolds, T. B. 2015. *Candida albicans* OPI1 regulates filamentous growth and virulence in vaginal infections, but not inositol biosynthesis. *PLoS One* 10: e0116974.
- Chorlay, A., Thiam, A. R. 2020. Neutral lipids regulate amphipathic helix affinity for model lipid droplets. *J. Cell Biol.* 219: e201907099.
- Choudhary, V., Ojha, N., Golden, A., Prinz, W. A. 2015. A conserved family of proteins facilitates nascent lipid droplet budding from the ER. *J. Cell Biol.* 211: 261-271.
- Choudhary, V., El Atab, O., Mizzon, G., Prinz, W. A., Schneiter, R. 2020. Seipin and Nem1 establish discrete ER subdomains to initiate yeast lipid droplet biogenesis. *J. Cell. Biol.* 219: e201910177.

- Čopič, A., Antoine-Bally, S., Giménez-Andrés, M., La Torre Garay, C., Antonny, B., Manni, M. M., Pagnotta, S., Guihot, J., Jackson, C. L. 2018. A giant amphipathic helix from a perilipin that is adapted for coating lipid droplets. *Nat. Commun.* 9: 1332.
- Currie, E., Guo, X., Christiano, R., Chitraju, C., Kory, N., Harrison, K., Haas, J., Walther, T. C., Farese, R. V Jr. 2014. High confidence proteomic analysis of yeast LDs identifies additional droplet proteins and reveals connections to dolichol synthesis and sterol acetylation. *J. Lipid Res.* 55: 1465-1467.
- da Silva Ferreira, M.E., Malavazi, I., Savoldi, M., Brakhage, A. A., Goldman, M. H., Kim, H. S., Nierman, W. C., Goldman, G. H. 2006. Transcriptome analysis of *Aspergillus fumigatus* exposed to voriconazole. *Curr. Genet.* 50: 32-44.
- Du, X., Zhou, L., Aw, Y. C., Mak, H. Y., Xu, Y., Rae, J., Wang, W., Zadoorian, A., Hancock, S. E., Osborne, B., Chen, X., Wu, J. W., Turner, N., Parton, R. G., Li, P., Yang, H. 2020. ORP5 localizes to ER-lipid droplet contacts and regulates the level of PI(4)P on lipid droplets. *J. Cell Biol.* 219: e201905162.
- Dubey, R., Stivala, C. E., Nguyen, H. Q., Goo, Y. H., Paul, A., Carette, J. E., Trost, B. M., Rohatgi, R. 2020. Lipid droplets can promote drug accumulation and activation. *Nat. Chem. Biol.* 16: 206-213.
- Dzurendova, S., Losada, C. B., Dupuy-Galet, B. X., Fjær, K., Shapaval, V. 2022. Mucoromycota fungi as powerful cell factories for modern biorefinery. *Appl. Microbiol. Biotechnol.* 106: 101-115.
- Eisenberg, D., Weiss, R. M., Terwilliger, T. C. 1982. The helical hydrophobic moment: a measure of the amphiphilicity of a helix. *Nature* 299: 371-374.
- Fei, W., Shui, G., Gaeta, B., Du, X., Kuerschner, L., Li, P., Brown, A. J., Wenk, M. R., Parton, R. G., Yang, H. 2008. Fld1p, a functional homologue of human seipin, regulates the size of lipid droplets in yeast. *J. Cell Biol.* 180:473-82.
- Gautier, R., Douguet, D., Antonny, B., Drin, G. 2008. HELIQUEST: a web server to screen sequences with specific alpha-helical properties. *Bioinformatics.* 24: 2101-2102.
- Greenspan, P., Mayer, E. P. & Fowler, S. D. 1985. Nile red: a selective fluorescent stain for intracellular lipid droplets. *J. Cell Biol.* 100: 965-973.
- Guo, Y., Walther, T. C., Rao, M., Stuurman, N., Goshima, G., Terayama, K., Wong, J. S., Vale, R. D., Walter, P., Farese, R. V. 2008. Functional genomic screen reveal genes involved in lipid-droplet formation and utilization. *Nature* 453: 657-661.

- Heyken, W. T., Repenning, A., Kumme, J., Schüller, H. J. 2005. Constitutive expression of yeast phospholipid biosynthetic genes by variants of Ino2 activator defective for interaction with Opi1 repressor. *Mol. Microbiol.* 56: 696-707.
- Hernández-Salmerón, J. E., Moreno-Hagelsieb, G. 2020. Progress in quickly finding orthologs as reciprocal best hits: comparing blast, last, diamond and MMseqs2. *BMC Genomics* 21: 741.
- Hinson, E. R., Cresswell, P. 2009. The antiviral protein, viperin, localizes to lipid droplets via its N-terminal amphipathic alpha-helix. *Proc. Natl. Acad. Sci. U S A.* 106: 20452-20457.
- Hirakawa, K., Kobayashi, S., Inoue, T., Endoh-Yamagami, S., Fukuda, R., Ohta, A. 2009. Yas3p, an Opi1 family transcription factor, regulates cytochrome P450 expression in response to n-alkanes in *Yarrowia lipolytica*. *J. Biol. Chem.* 284: 7126-137.
- Hofbauer, H. F., Gecht, M., Fischer, S. C., Seybert, A., Frangakis, A. S., Stelzer, E. H. K., Covino, R., Hummer, G., Ernst, R. 2018. The molecular recognition of phosphatidic acid by an amphipathic helix in Opi1. *J. Cell Biol.* 217: 3109-3126.
- Jacquier, N., Choudhary, V., Mari, M., Toulmay, A., Reggiori, F., Schneider, R. 2011. Lipid droplets are functionally connected to the endoplasmic reticulum in *Saccharomyces cerevisiae*. *J. Cell. Sci.* 124: 2424-2437.
- Joshi, A. S., Nebenfuhr, B., Choudhary, V., Satpute-Krishnan, P., Levine, T. P., Golden, A., Prinz, W. A. 2018. Lipid droplet and peroxisome biogenesis occur at the same ER subdomains. *Nat. Commun.* 9: 2940.
- Kaminskyj, S. G., Hamer, J. E. 1998. hyp loci control cell pattern formation in the vegetative mycelium of *Aspergillus nidulans*. *Genetics.* 148: 669-680.
- Kelley, L., Mezulis, S., Yates, C., Wass, M. N., Sternberg, M. J. 2015. The Phyre2 web portal for protein modeling, prediction and analysis. *Nat Protoc* 10: 845–858.
- Kiss, E., Hegedüs, B., Virágh, M., Varga, T., Merényi, Z., Kószó, T., Bálint, B., Prasanna, A. N., Krizsán, K., Kocsubé, S., Riquelme, M., Takeshita, N., Nagy, L. G. 2019. Comparative genomics reveals the origin of fungal hyphae and multicellularity. *Nat. Commun.* 10: 4080.
- Kosa, G., Zimmermann, B., Kohler, A., Ekeberg, D., Afseth, N. K., Mounier, J., Shapaval, V. 2018. High-throughput screening of Mucoromycota fungi for production of low- and high-value lipids. *Biotechnol. Biofuels* 11: 66.
- Kosugi, S., Hasebe, M., Tomita, M., Yanagawa H. 2009. Systematic identification of cell cycle-dependent yeast nucleocytoplasmic shuttling proteins by prediction of composite motifs. *Proc. Natl. Acad. Sci. U S A.* 106: 10171-10176.

- Kory, N., Thiam, A. R., Farese, R. V. Jr., Walther, T. C. 2015. Protein Crowding Is a Determinant of Lipid Droplet Protein Composition. *Dev. Cell.* 34: 351-363.
- Kumar, S., Stecher, G., & Tamura, K. 2016. MEGA7: Molecular Evolutionary Genetics Analysis Version 7.0 for Bigger Datasets. *Mol. Biol. Evol.* 33: 1870–1874.
- Lawton, M. P., Cashman, J. R., Cresteil, T., Dolphin, C. T., Elfarra, A. A., Hines, R. N., Hodgson, E., Kimura, T., Ozols, J., Phillips, I. R. 1994. A nomenclature for the mammalian flavin-containing monooxygenase gene family based on amino acid sequence identities. *Arch. Biochem. Biophys.* 308: 254–257.
- Li, L., Stoeckert, C. J Jr., Roos, D. S. 2003. OrthoMCL: identification of ortholog groups for eukaryotic genomes. *Genome Res.* 13: 2178-89.
- Listenberger, L. L., Ostermeyer-Fay, A. G., Goldberg, E. B., Brown, W. J., Brown, D. A. 2007. Adipocyte differentiation-related protein reduces the lipid droplet association of adipose triglyceride lipase and slows triacylglycerol turnover. *J. Lipid Res.* 48: 2751-2761.
- Liu, H. L., De Souza, C. P., Osmani, A. H., Osmani, S. A. 2009. The three fungal transmembrane nuclear pore complex proteins of *Aspergillus nidulans* are dispensable in the presence of an intact An-Nup84-120 complex. *Mol. Biol. Cell* 20: 616-630.
- Loewen, C.J., Gaspar, M.L., Jesch, S.A., Delon, C., Ktistakis, N.T., Henry, S.A., and Levine, T.P. 2004. Phospholipid metabolism regulated by a transcription factor sensing phosphatidic acid. *Science* 304: 1644–1647.
- Mamun, M. A. A., Katayama, T., Cao, W., Nakamura, S., Maruyama, J. I. 2020. A novel Pezizomycotina-specific protein with gelsolin domains regulates contractile actin ring assembly and constriction in perforated septum formation. *Mol. Microbiol.* 113: 964–982.
- *Mamun, M. A. A., Katayama T, Cao W, Nakamura S, Maruyama JI. 2022. Multiple genes evolved for fungal septal pore plugging identified via large-scale localization and functional screenings. *bioRxiv.* doi.org/10.1101/2022.11.24.517796 (Preprint posted November 24, 2022)
- Markina-Iñarrairaegui, A., Pantazopoulou, A., Espeso, E.A., Peñalva, M. A. 2013. The *Aspergillus nidulans* peripheral ER: disorganization by ER stress and persistence during mitosis. *PLoS One.* 8: e67154.
- Maruyama, J., and Kitamoto, K. 2011. Targeted gene disruption in *Koji* mold *Aspergillus oryzae*. *Methods Mol. Biol.* 765: 447–456.
- Mirdita, M., Schütze, K., Moriwaki, Y., Heo, L., Ovchinnikov, S., Steinegger, M. 2022. ColabFold: making protein folding accessible to all. *Nat Methods* 19: 679–682.

- Monson, E. A., Crosse, K. M., Duan, M., Chen, W., O'Shea, R. D., Wakim, L. M., Carr, J. M., Whelan, D. R., Helbig, K. J. 2021. Intracellular lipid droplet accumulation occurs early following viral infection and is required for an efficient interferon response. *Nat. Commun.* 12: 4303.
- Munson, M., Anderson, K. S., Regan, L. 1997. Speeding up protein folding: mutations that increase the rate at which Rop folds and unfolds by over four orders of magnitude. *Fold. Des.* 2: 77-87.
- Naranjo-Ortiz, M. A., Gabaldón, T. 2019. Fungal evolution: major ecological adaptations and evolutionary transitions. *Biol. Rev. Camb. Philos. Soc.* 94: 1443-1476.
- Negishi, M., Pedersen, L. G., Petrotchenko, E., Shevtsov, S., Gorokhov, A., Kakuta, Y., Pedersen, L. C. 2001. Structure and function of sulfotransferases. *Arch. Biochem. Biophys.* 390: 149-157.
- Nguyen, T. A., Cissé, O. H., Yun Wong, J., Zheng, P., Hewitt, D., Nowrousian, M., Stajich, J. E., & Jedd, G. 2017. Innovation and constraint leading to complex multicellularity in the Ascomycota. *Nat. Commun.* 8: 14444.
- Novo, M., Bigey, F., Beyne, E., Galeote, V., Gavory, F., Mallet, S., Cambon, B., Legras, J. L., Wincker, P., Casaregola, S., Dequin, S. 2009. Eukaryote-to-eukaryote gene transfer events revealed by the genome sequence of the wine yeast *Saccharomyces cerevisiae* EC1118. *Proc. Natl. Acad. Sci. U S A.* 106: 16333-16338.
- Olarte, M. J., Kim, S., Sharp, M. E., Swanson, J. M. J., Farese, R. V. Jr., Walther, T. C. 2020. Determinants of Endoplasmic Reticulum-to-Lipid Droplet Protein Targeting. *Dev. Cell.* 54: 471-487.e7.
- Olzmann, J. A., and Carvalho P. 2019. Dynamics and functions of lipid droplets. *Nat. Rev. Mol. Cell Biol.* 20:137-155.
- Pataki, C. I., Rodrigues, J., Zhang, L., Qian, J., Efron, B., Hastie, T., Elias, J. E., Levitt, M., Kopito, R. R. 2018. Proteomic analysis of monolayer-integrated proteins on lipid droplets identifies amphipathic interfacial α -helical membrane anchors. *Proc. Natl. Acad. Sci. U S A.* 115: E8172-E8180.
- Prévost, C., Sharp, M. E., Kory, N., Lin, Q., Voth, G. A., Farese, R. V. Jr., Walther, T. C. 2018. Mechanism and Determinants of Amphipathic Helix-Containing Protein Targeting to Lipid Droplets. *Dev. Cell.* 44: 73-86.
- Pronk, J. T., Yde Steensma, H., Van Dijken, J. P. 1996. Pyruvate metabolism in *Saccharomyces cerevisiae*. *Yeast* 12: 1607-1633.
- Qiu, B., Simon, M. C. 2016. BODIPY 493/503 Staining of Neutral Lipid Droplets for Microscopy and Quantification by Flow Cytometry. *Bio. Protoc.* 6: e1912.

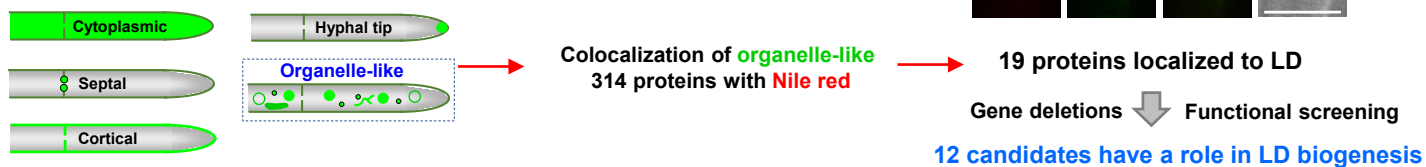
- Revie, N. M., Iyer, K. R., Robbins, N., Cowen LE. 2018. Antifungal drug resistance: evolution, mechanisms and impact. *Curr. Opin. Microbiol.* 45: 70-76.
- Romanuska, A and Köhler, A. 2018. The Inner Nuclear Membrane Is a Metabolically Active Territory that Generates Nuclear Lipid Droplets. *Cell.* 174: 700-715
- Roundtree, M. T., Juvvadi, P. R., Shwab, E. K., Cole, D. C., Steinbach, W. J. 2020. *Aspergillus fumigatus* Cyp51A and Cyp51B Proteins Are Compensatory in Function and Localize Differentially in Response to Antifungals and Cell Wall Inhibitors. *Antimicrob. Agents. Chemother.* 64: e00735-20.
- Rowe, E. R., Mimmack, M. L., Barbosa, A. D., Haider, A., Isaac, I., Ouberai, M. M., Thiam, A. R., Patel, S., Saudek, V., Siniosoglou, S., Savage, D. B. 2016. Conserved Amphipathic Helices Mediate Lipid Droplet Targeting of Perilipins 1-3. *J. Biol. Chem.* 291: 6664-6678.
- Schneider, C.A., Rasband, W.S., Eliceiri, K.W. 2012. NIH Image to ImageJ: 25 years of image analysis. *Nat. Methods* 9: 671-675.
- Schultz, J., Milpetz, F., Bork, P., & Ponting, C. P. 1998. SMART, a simple modular architecture research tool: Identification of signaling domains. *Proc. Natl. Acad. Sci. USA* 95: 5857–5864.
- Shen, X. X., Steenwyk, J. L., LaBella, A. L., Opulente, D. A., Zhou, X., Kominek, J., Li, Y., Groenewald, M., Hittinger, C. T., Rokas, A. 2020. Genome-scale phylogeny and contrasting modes of genome evolution in the fungal phylum Ascomycota. *Sci Adv.* 6: eabd0079.
- Sołtysik, K., Ohsaki, Y., Tatematsu, T., Cheng, J., Maeda, A., Morita, S. Y., Fujimoto, T. 2021. Nuclear lipid droplets form in the inner nuclear membrane in a seipin-independent manner. *J. Cell. Biol.* 220: e202005026.
- Suelmann, R., Sievers, N., Fischer, R. 1997. Nuclear traffic in fungal hyphae: in vivo study of nuclear migration and positioning in *Aspergillus nidulans*. *Mol. Microbiol.* 25: 757-769.
- Sun, X., Wang, K., Yu, X., Liu, J., Zhang, H., Zhou, F., Xie, B., Li, S. 2014. Transcription factor CCG-8 as a new regulator in the adaptation to antifungal azole stress. *Antimicrob. Agents Chemother* 58:1434-1442.
- Szymanski, K. M. Binns, D., Bartz, R., Grishin, N. V., Li, W. P., Agarwal, A. K, Garg, A., Anderson, R. G., Goodman, J. M. 2007. The lipodystrophy protein seipin is found at endoplasmic reticulum lipid droplet junctions and is important for droplet morphology. *Proc. Natl. Acad. Sci. U S A.* 104: 20890-20895.

- Taneva, S. G., Lee, J. M., Cornell, R. B. 2012. The amphipathic helix of an enzyme that regulates phosphatidylcholine synthesis remodels membranes into highly curved nanotubules. *Biochim. Biophys. Acta.* 1818: 1173-1186.
- Thompson, J. D., Gibson, T. J., and Higgins, D. G. 2002. Multiple Sequence Alignment Using ClustalW and ClustalX. *Curr. Protoc. Bioinformatics.* Chapter 2: Unit 2.3.
- van Zutphen, T., Todde, V., de Boer, R., Kreim, M., Hofbauer, HF., Wolinski, H., Veenhuis, M., van der Klei, I.J., Kohlwein, S, D. 2014. Lipid droplet autophagy in the yeast *Saccharomyces cerevisiae*. *Mol. Biol. Cell.* 25: 290-301.
- Walther, T. C., Chung, J., and Farese, R. V. Jr. 2017. Lipid Droplet Biogenesis. *Annu. Rev. Cell Dev. Biol.* 33: 491-510.
- Wang, L., Walsh, M. T., and Small, D. M. 2006. Apolipoprotein B is conformationally flexible but anchored at a triolein/water interface: a possible model for lipoprotein surfaces. *Proc. Natl. Acad. Sci. U S A.* 103: 6871-6876.
- Ward, N., and Moreno-Hagelsieb, G. 2014. Quickly finding orthologs as reciprocal best hits with BLAT, LAST, and UBLAST: how much do we miss? *PLoS One* 9: e101850.
- Welte, M. A. 2015. Expanding roles for lipid droplets. *Curr. Biol.* 25: R470-481.
- Wisecaver, J. H., Slot, J. C., and Rokas, A. 2014. The evolution of fungal metabolic pathways. *PLoS Genet.* 10: e1004816.
- Xu, Y., Chen, J., Chen, J., Teng, J. 2022. EI24 promotes cell adaption to ER stress by coordinating IRE1 signaling and calcium homeostasis. *EMBO Rep.* 23: e51679.

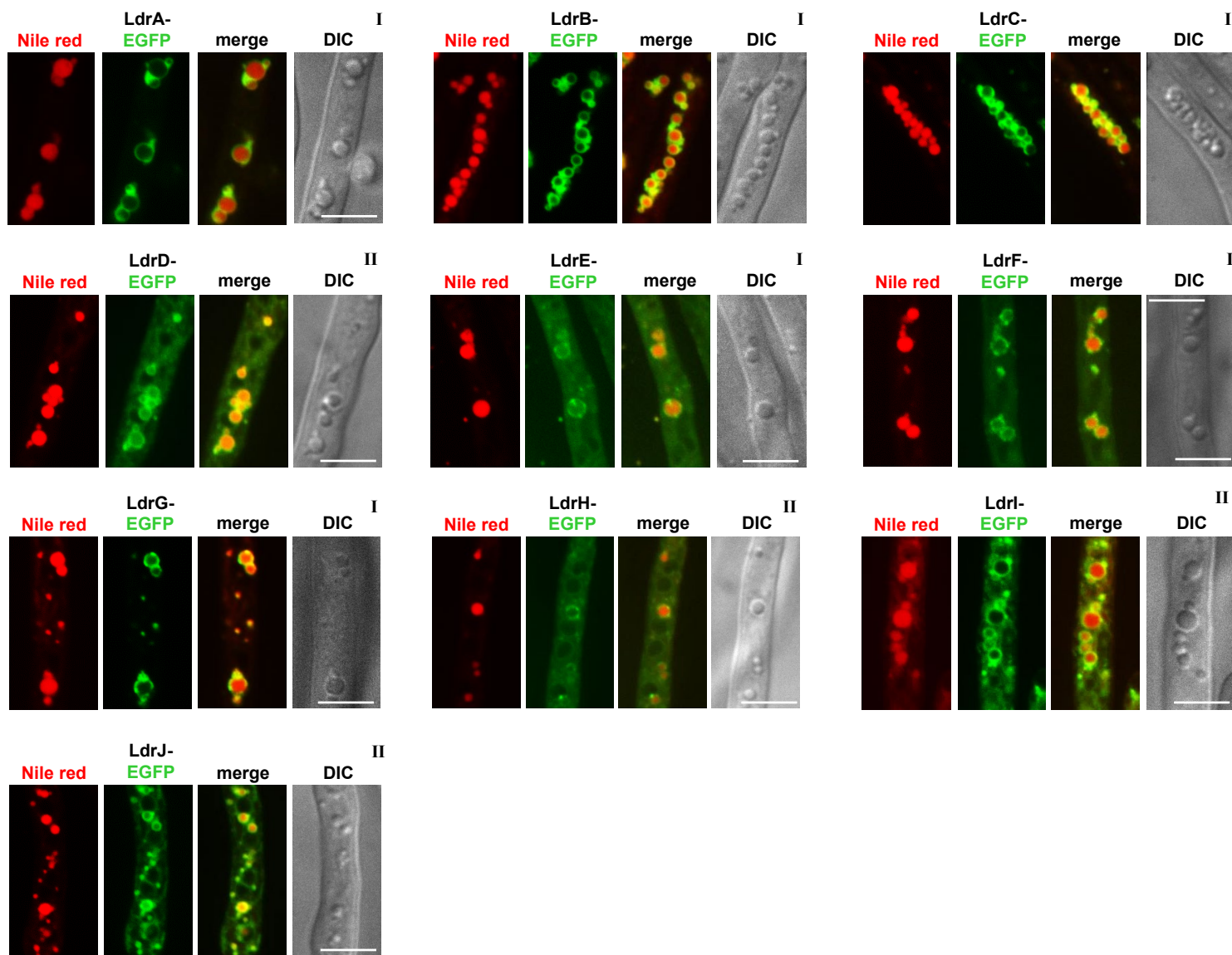
*The manuscript is now under revisions stage in *Nature communications* (NCOMMS-22-01369A)

A

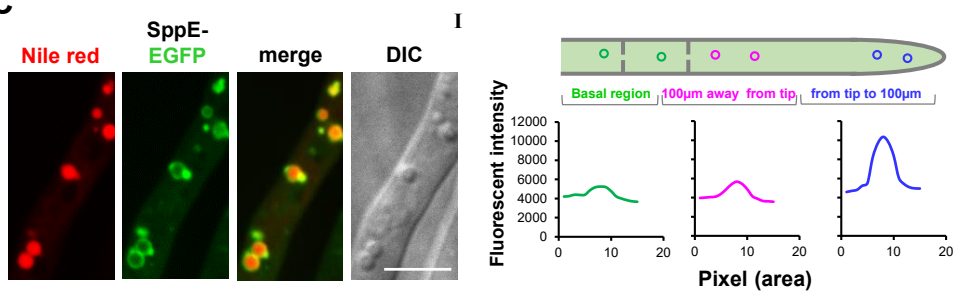
EGFP fused protein library
<https://doi.org/10.1101/2022.11.24.517872>; this version posted November 20, 2022. The copyright holder for this preprint (which was not certified by peer review) is the author/funder. All rights reserved. No reuse allowed without permission.



B



C



D

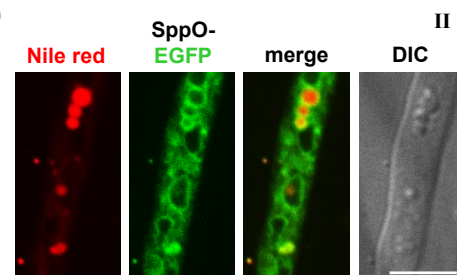
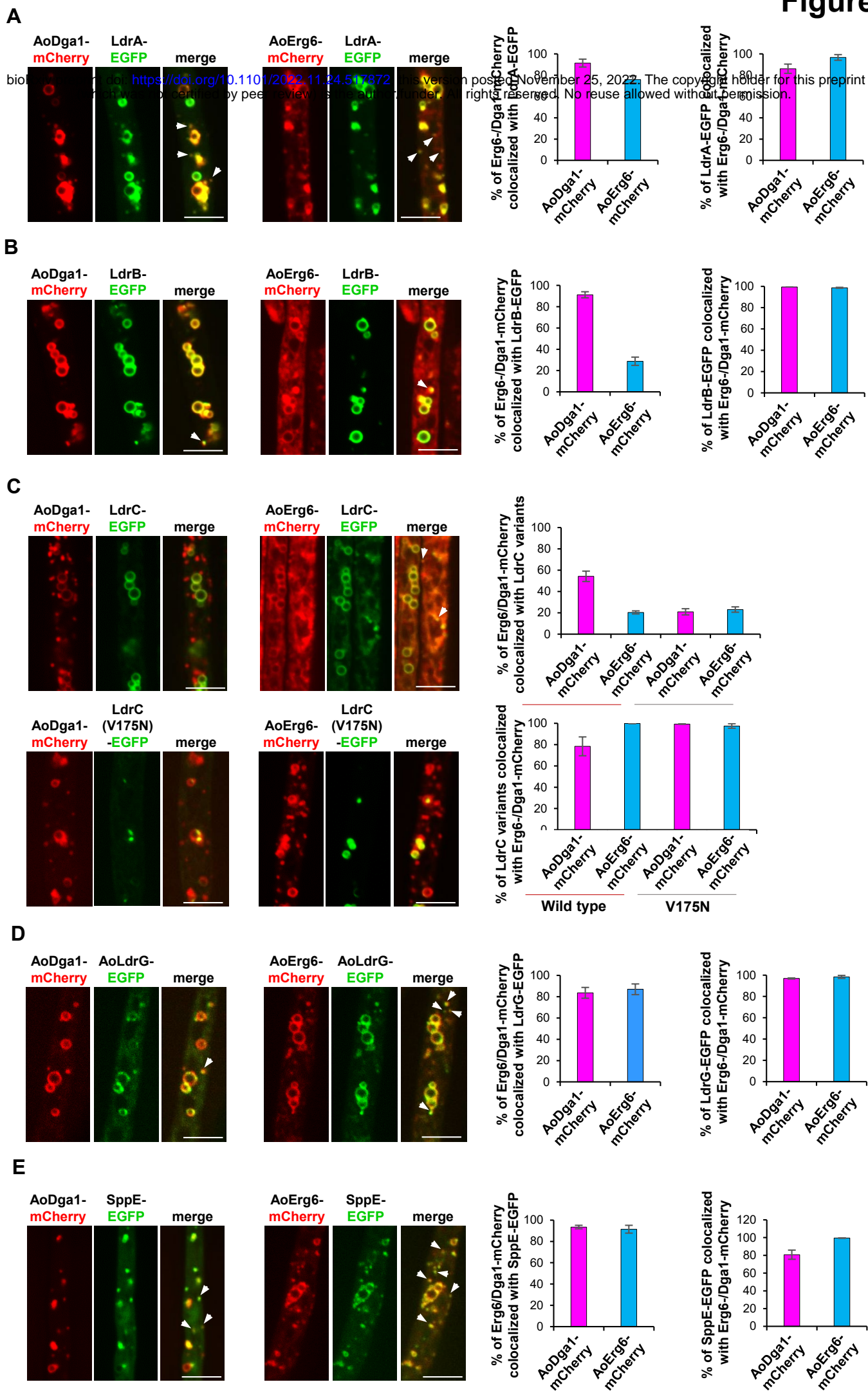


Figure 1. Colocalization screening identifies a set of novel proteins associated with lipid droplets.

(A) Schematic representation of the overall strategies involved in the reverse genetic approach including localization and functional screening to identify novel proteins that regulate LD dynamics. (B-D) Fluorescence microscopy images of *C. albicans* expressing EGFP-fused LDR, and two FCC proteins, were expressed under the control of heterologous *amyB* promoters. Colocalization of EGFP-fused proteins with Nile red was observed from living cells cultured on the minimal medium for 18 h. Fungal hyphae were stained with 10 μ g/mL Nile red for the visualization of LD. Type I represents proteins exclusively localized on LD and type II denotes shared localization including LD and other organelles. The representative microphotographs are shown. Bars 5 μ m. (C) Diverse LD-binding affinity FccF-EGFP along the hyphae. Y-axis indicates the mean fluorescent intensity of FccF-EGFP on LD-membrane captured from three different regions of hyphae. n = 20.



bioRxiv preprint doi: <https://doi.org/10.1101/2022.11.24.517872>; this version posted November 25, 2022. The copyright holder for this preprint (which was not certified by peer review) is the author/funder, who has granted bioRxiv a license to display the preprint in perpetuity. It is made available under aCC-BY 4.0 International license.

Figure 2. LDR and SppE proteins colocalized with nascent LD marker proteins Erg6 and Dga1

bioRxiv preprint doi: <https://doi.org/10.1101/2022.11.24.517872>; this version posted November 25, 2022. The copyright holder for this preprint (which was not certified by peer review) is the author/funder. All rights reserved. No reuse allowed without permission.

Aoerg6-mCherry and alternatively AoDga1-mCherry under the control of *amyB* promoter were ectopically introduced into the wild-type. Previously developed EGFP-tagged LDR proteins under the control of heterologous *amyB* promoter were further ectopically introduced onto the resultant. Strains were cultured on the minimal medium with optimized carbon concentration. Bars 5 μ m. Arrowheads represent the colocalization points as small-sized puncta. The percentage of AoErg6-mCherry and AoDga1-mCherry associated with EGFP-tagged LDR proteins were automatically calculated using ImageJ. Data are presented as mean \pm SD, n = 12 hyphae. **(A)**, **(B)**, **(C)**, **(D)**, and **(E)** colocalization analysis of Aoerg6-mCherry, alternatively, AoDga1-mCherry with LdrA-EGFP, LdrB-EGFP, LdrC-EGFP, LdrG-EGFP, and FccE-EGFP variants, respectively.

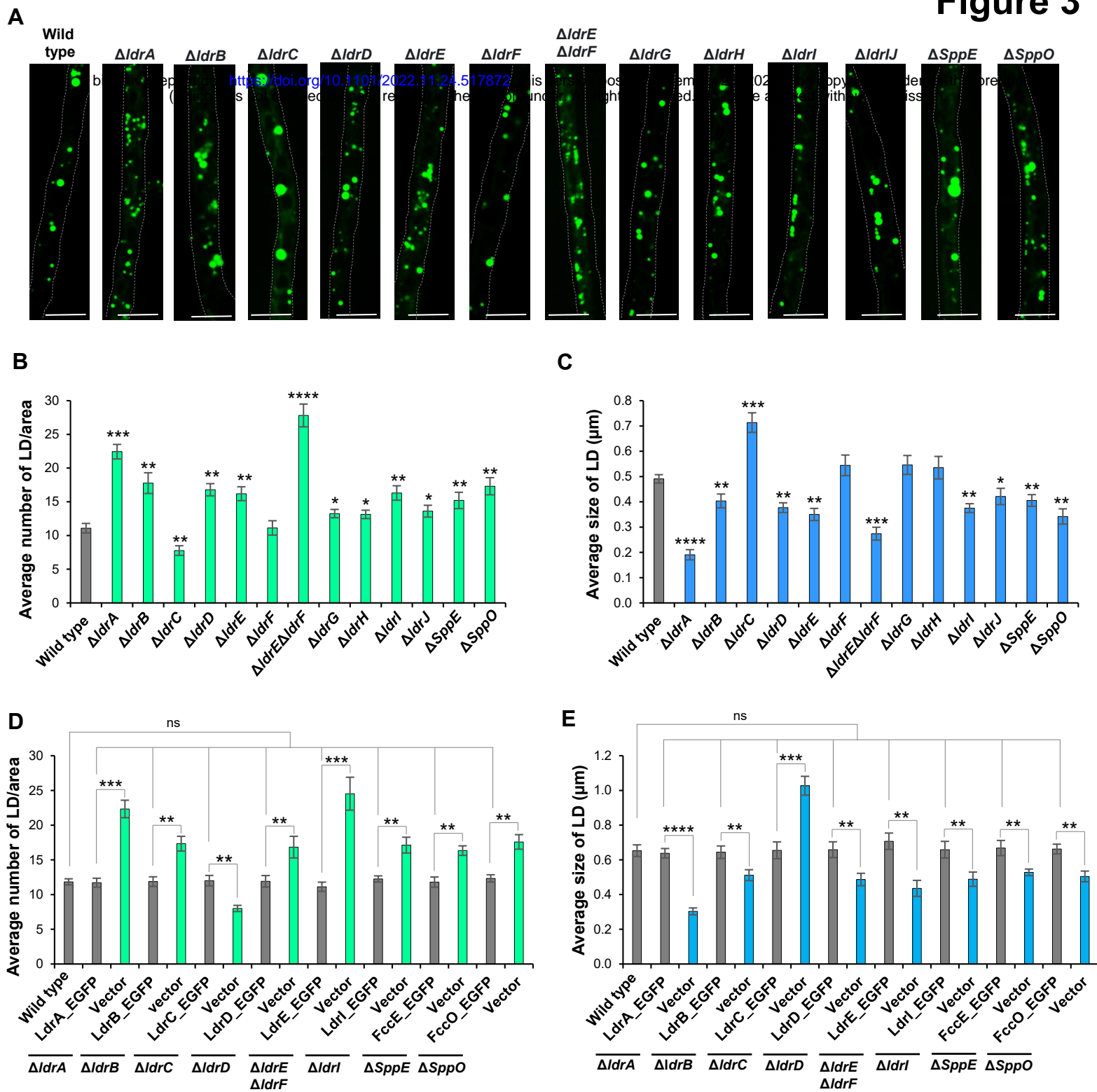


Figure 3. Single and double deletions of LDR proteins, as well as FCC proteins, resulted in abnormal LD biogenesis

LD was quantitatively analyzed from living hyphae cultured in the M minimal medium for 20 h. Fungal hyphae were stained with 5 μm BODIPY 494/503 (A) Representative microphotographs of BODIPY-stained LD observed in wild-type and gene deletions were shown. Dotted lines represent the hyphal periphery. Bars 5 μm. (B) Quantification of average LD number per hyphal area (45 μm) from ≥ 37 fungal hyphae. (C) Automated quantification of average LD size using ImageJ. n ≥ 354 LD. (D-E) Deletions and double deletions were complemented with respective full-length gene sequences tagged with EGFP and expressed from the corresponding endogenous promoter. Positive (wild-type) and negative (vector integration) controls are developed with a similar auxotrophic background. (D) Quantification of average LD number per hyphal area (45 μm) from ≥ 24 fungal hyphae. (E) Automated quantification of average LD size using ImageJ. n ≥ 313 LD. (B-E) Results are represented as the mean value from three independent experiments. Statistical significance was evaluated using two-sampled student *t-test*. Error bars represent SD. ns-not significant p > 0.05, *p < 0.05, **p < 0.01, ***p < 0.001, ****p < 0.0001

Figure 4

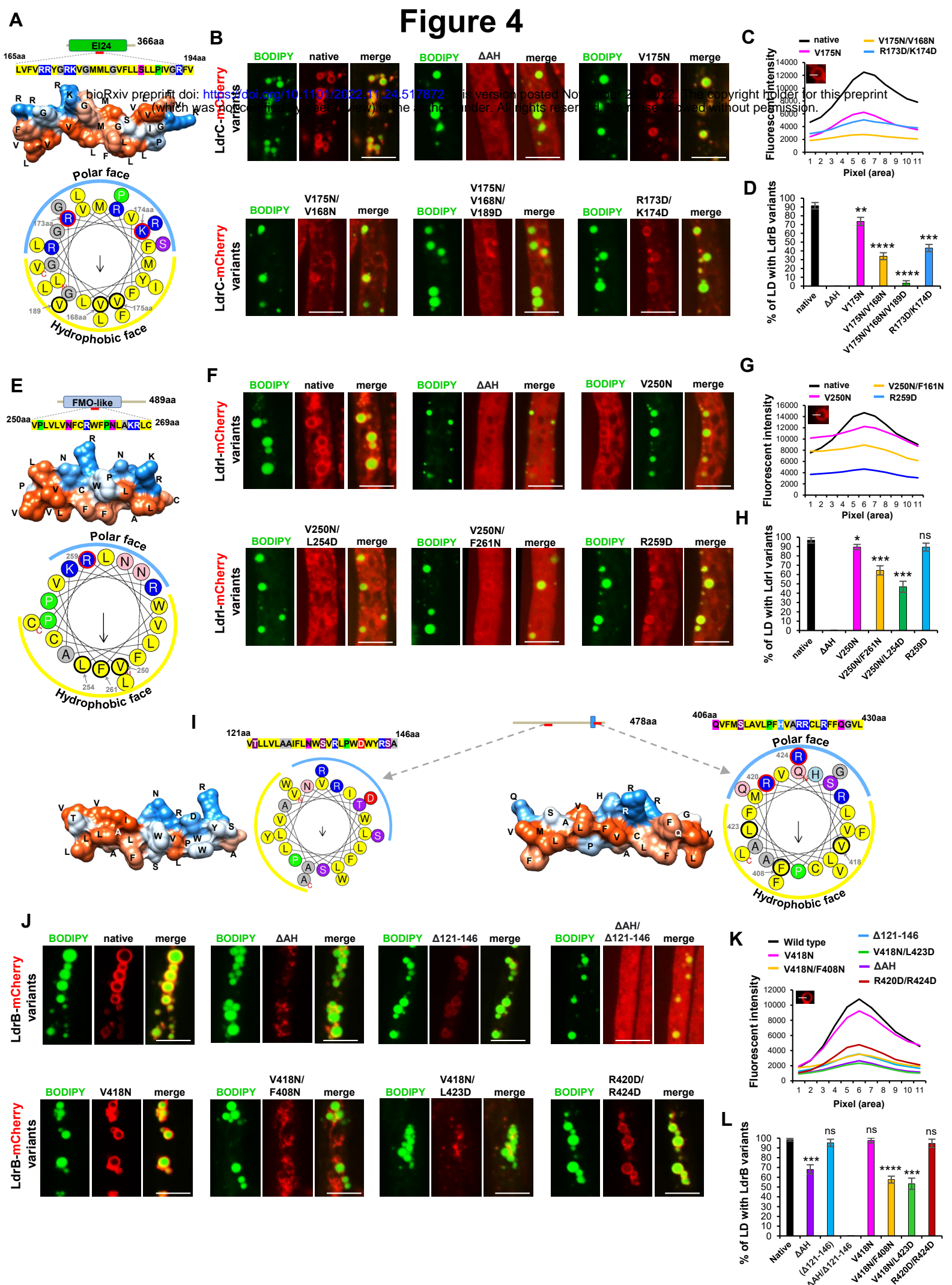


Figure 4. Influence of hydrophobicity and charge of the putative AHs present in the LdrB, LdrC, and LdrI to selectively

target LD bioRxiv preprint doi: <https://doi.org/10.1101/2022.11.24.517872>; this version posted November 25, 2022. The copyright holder for this preprint (which was not certified by peer review) is the author/funder. All rights reserved. No reuse allowed without permission.

(A), (E), and (I) helical wheels and predicted 3D model of α -helical representation of AH. Amino acid properties and positions are indicated by colors and numbers, respectively. Hydrophobic and polar faces are shown with orange and blue curve lines, respectively. **(B), (F), and (J)** $\Delta ldrC$, $\Delta ldrI$, and $\Delta ldrB$ were complemented with mCherry-fused corresponding wild-type and AH-disrupting mutational variants from heterologous *amyB* promoter, respectively. Hyphae cultured on minimal medium (CD) were stained with BODIPY. Representative microphotographs are shown. Bars 5 μm . **(C), (G), and (K)** Mean fluorescent intensity of the mCherry-fused variants of LdrB, LdrC, and LdrI captured from the LD membrane, respectively. Fluorescent intensity was measured by drawing a transverse line on the LD membrane using ImageJ. $n = 20$ LD. **(D), (H), and (I)** Percentage of BODIPY-stained LD positive with LdrB, LdrC, and LdrI variants, respectively. Experiments were performed in triplicates. $n \geq 95$ LD. Statistical significance was assessed using two-sampled student *t-test*. Error bars represent SD. ns-not significant $p > 0.05$, * $p < 0.05$, ** $p < 0.01$, *** $p < 0.001$, **** $p < 0.0001$.

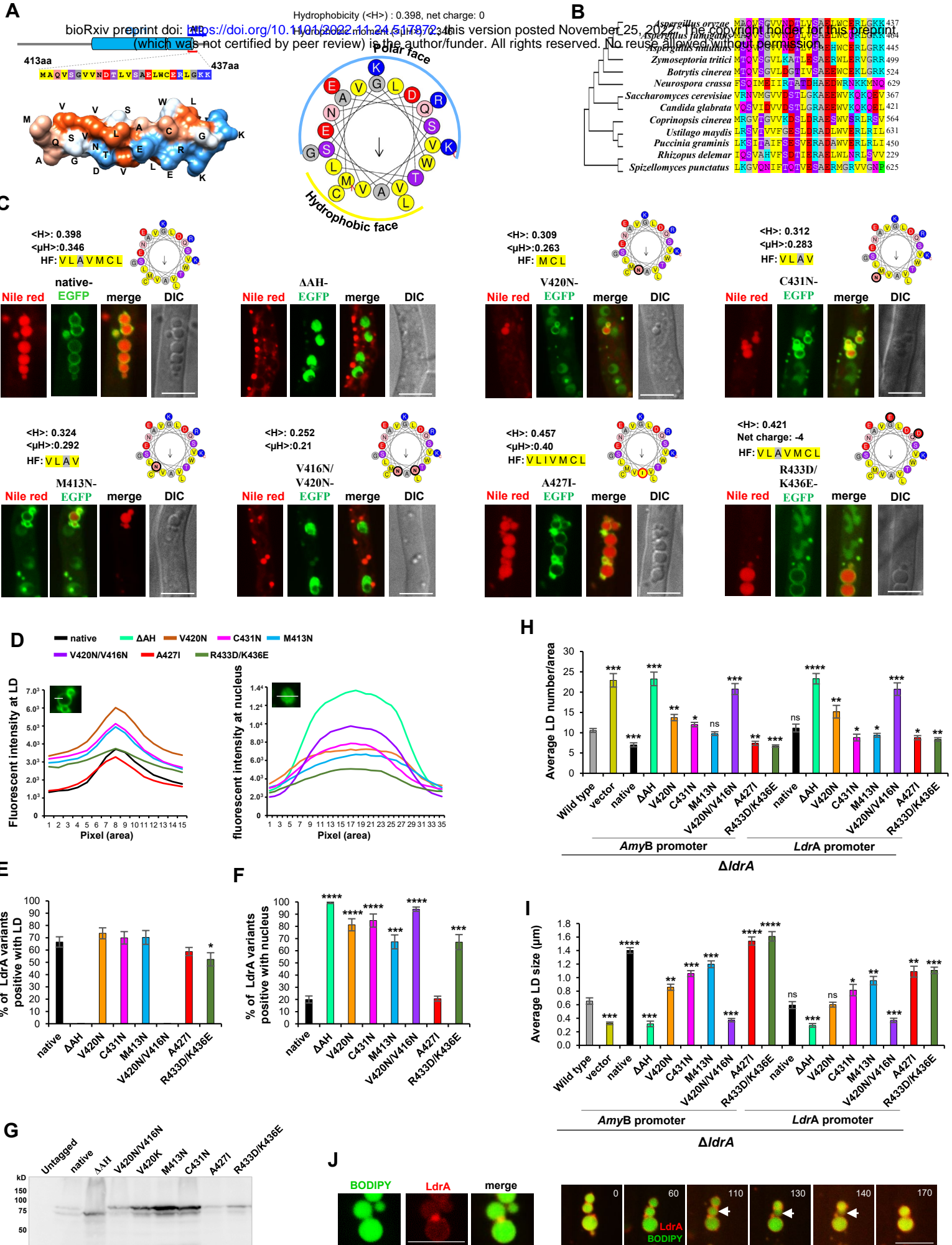
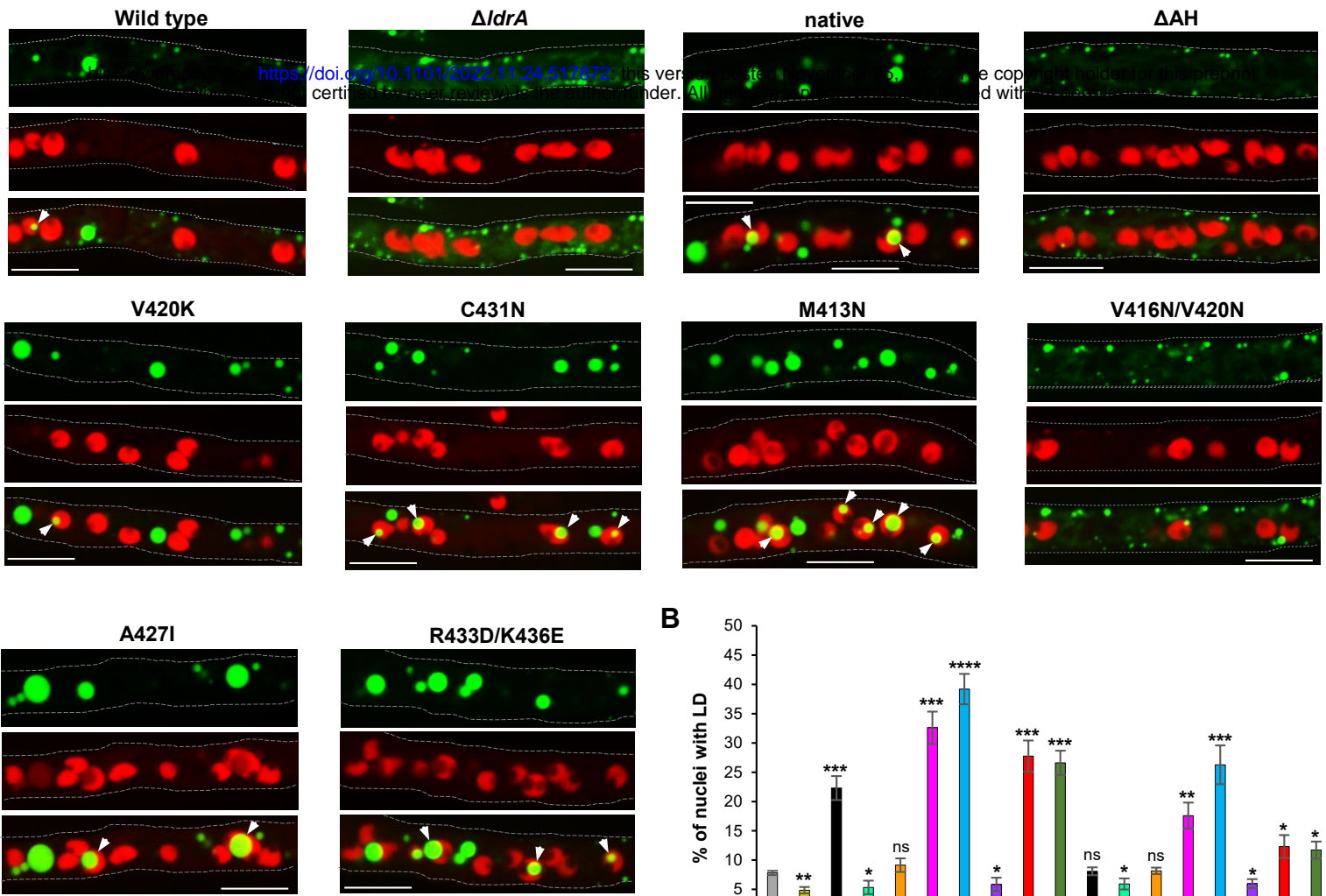


Figure 5. LdrA binds to and regulates LD biogenesis via the insertion of a novel C-terminus amphipathic helix

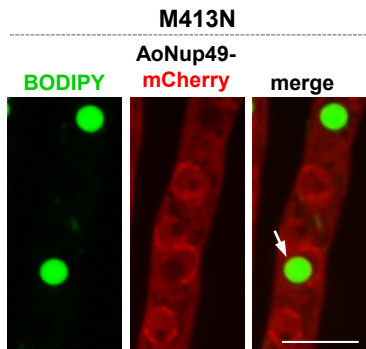
bioRxiv preprint doi: <https://doi.org/10.1101/2022.11.24.517872>; this version posted November 25, 2022. The copyright holder for this preprint (which was not certified by peer review) is the author/funder. All rights reserved. No reuse allowed without permission.

(A) Helical wheel representation of predicted AH using HelixQuest. Amino acid properties are indicated by colors. The 3D modeling of α -helix covering the putative AH is presented using AlfaFold2 and subsequent Chimera, version 1.16. Hydrophobic and polar faces are shown with orange and blue curve lines, respectively. (B) Multiple sequence alignment of AH from fungal orthologues. (C) Mutants designed to disrupt the amphipathic nature of AH were introduced into $\Delta ldrA$ from the heterologous *amyB* promoter. Live-cell imaging was performed from the variants cultured on the minimal medium (CD). Representative images were shown. (C-E) LD was visualized with 10 $\mu\text{g}/\text{mL}$ Nile red. Bars 5 μm . (D) Mean fluorescent intensity of EGFP-tagged variants of LdrA at nucleus and LD membrane. The intensity was calculated by drawing lines on the LD membrane or nucleus using ImageJ. N = 30. (E) Percentage of LD positive with LdrA variants. n \geq 221 Nile red-stained LD. (F) Percentage of nucleus positive with LdrA variants. For nuclear enrichment analysis, $\Delta ldrA$ ectopically expressing AoNup84-mCherry was complemented with EGFP-fused LdrA variants. n \geq 212 Nup84-marked nuclei. (G) Protein level in LdrA variants was detected by western blotting using anti-GFP antibody. (H-I) Quantification of average LD number per hyphal area (45 μm) and LD size from LdrA variants (no EGFP tagging), respectively. LD was visualized with BODIPY 493/503. (H) n \geq 27 hyphae. (I) n \geq 135 LD. The bar diagrams are represented as the mean value from three independent experiments. Statistical significance was assessed using two-sampled student *t-test*. Error bars represent SD. ns-not significant p > 0.05, *p < 0.05, **p < 0.01, ***p < 0.001, ****p < 0.0001. (J) LdrA accumulated at the LD-LD fusion site. Strain expressing LdrA-mCherry was stained with BODIPY. Time course observation of LD fusion (right). Arrowheads indicate ongoing fused LD. time= min.

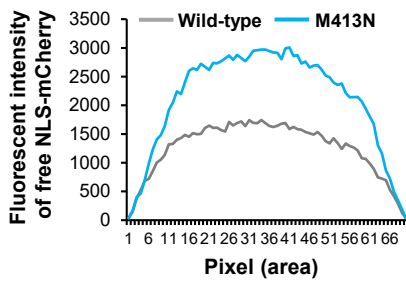
A



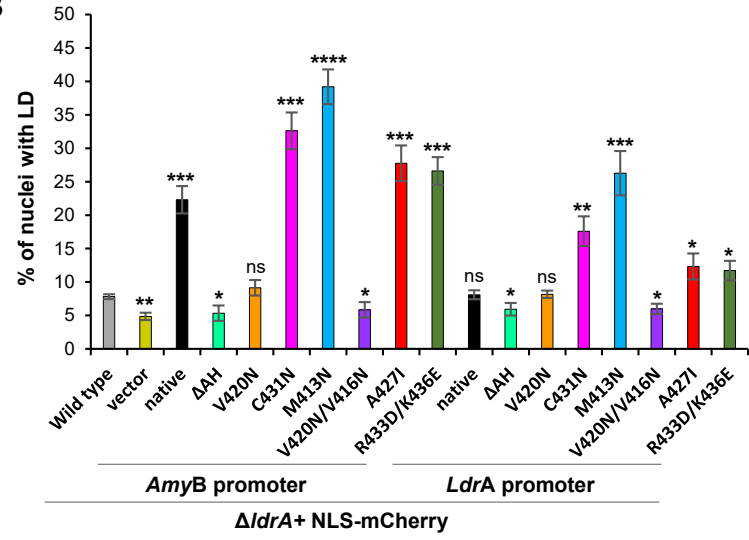
C



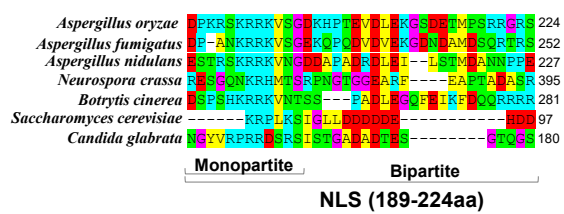
D



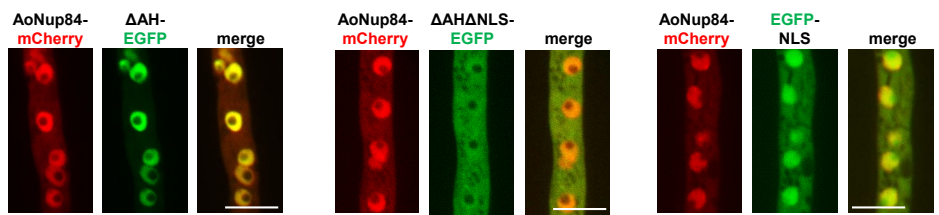
B



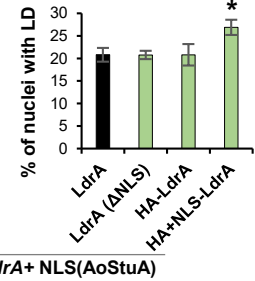
E



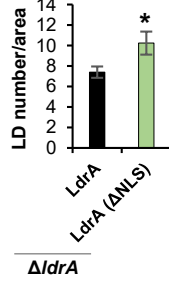
F



G



H



I

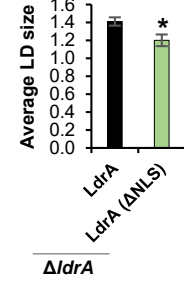
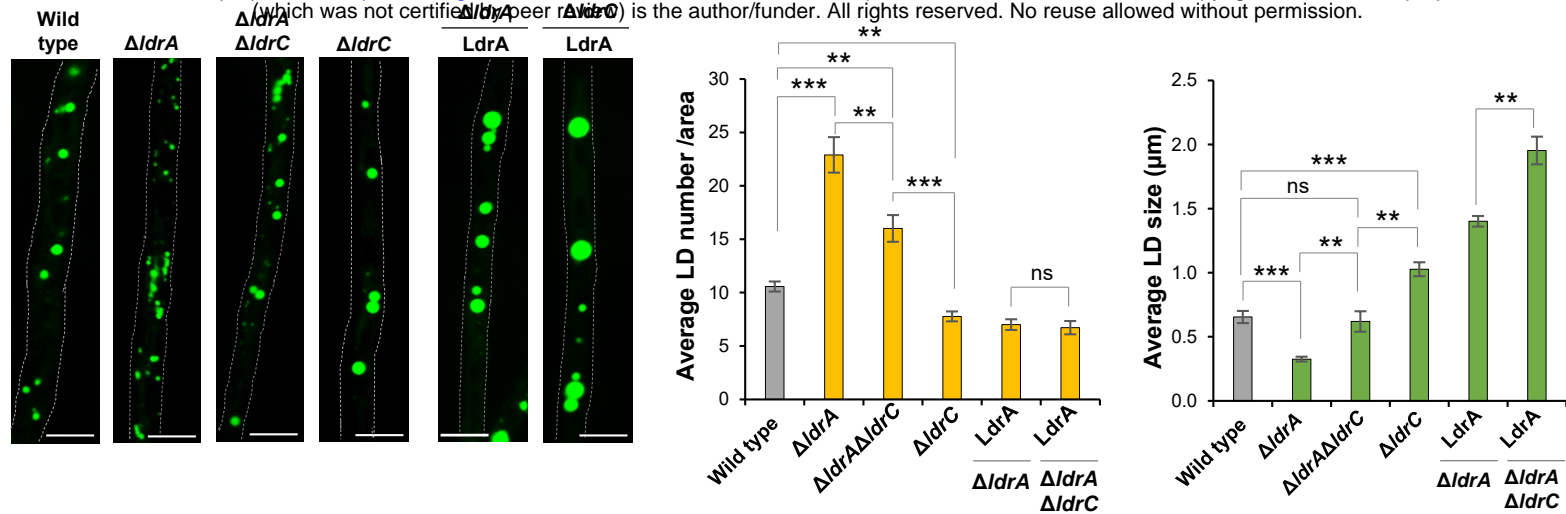


Figure 6. LdrA induced nuclear LD biogenesis

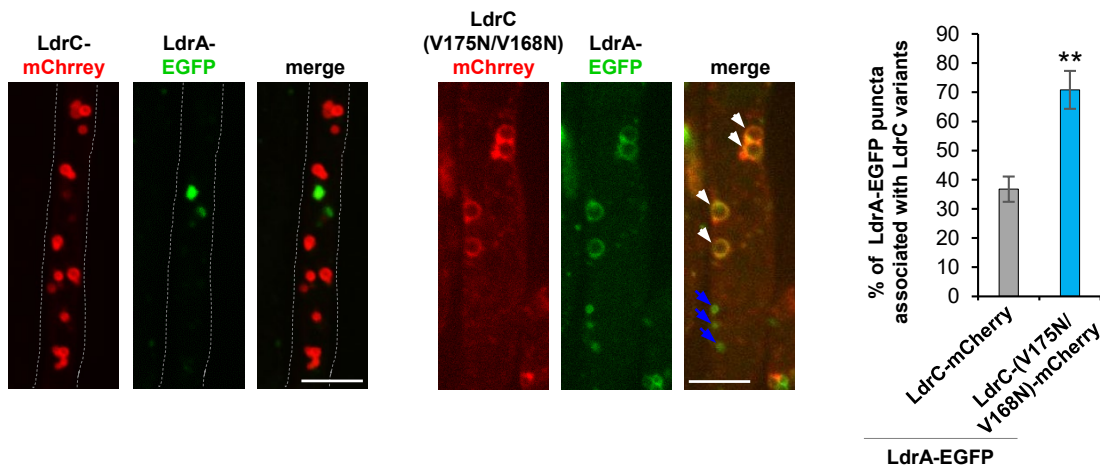
(A) Live-cell imaging from $\Delta ldrA$ +NLS-mCherry complemented with LdrA variants overexpressed by heterologous *amyB* promoter. Lds and nLds were identified by live imaging using BODIPY and NLS-mCherry, respectively. Representative images are shown. Arrowheads indicate nLD. Dotted lines represent the hyphal periphery. Bars 5 μ m. **(B)** LdrA variants were either expressed from its endogenous promoter or overexpressed from the heterologous *amyB* promoter. The bar diagrams showing the percentage of nLD are presented as the mean value from three independent experiments. $n \geq 216$ nuclei. Statistical significance was assessed using the two-sampled student *t-test*. Error bars represent SD. ns-not significant $p > 0.05$, * $p < 0.05$, ** $p < 0.01$, *** $p < 0.001$, **** $p < 0.0001$. **(C)** Disruption of nuclear periphery due to super-sized nLD. $\Delta ldrA$ +AoNup49-mCherry was complemented with M413A variant from overexpressed from *amyB* promoter. Arrow represents the disrupted nuclear periphery. Bars 5 μ m. **(D)** Mean fluorescent intensity of NLS-mCherry quantified from the cytoplasmic pool of M413N variants and wild-type. Background intensity was subtracted, and intercellular intensity was quantified using ImageJ by drawing the horizontal line transverse to the hyphae. **(E)** Prediction of NLS on LdrA using cNLS Mapper. Multiple sequence alignment covering the predicted NLS region among the fungal orthologues. Strains were cultured in CD agar medium supplemented with 1% casamino acids for 20 h. Bars 5 μ m. **(F)** Colocalization of EGFP-fused LdrA variants losing either predicted AH or the combination with NLS; as well as EGFP-NLS alone with AoNup84-mCherry. **(G)** Percentage of nuclei with LDs analyzed from LdrA variants in the presence and absence of NLS. $n \geq 240$ nuclei. **(H-I)** Quantification of average LD number (per area) and LD size from LdrA variants (no EGFP tagging), respectively. **(H)** $n \geq 32$ hyphal area and **(I)** $n \geq 217$ LD. **(G-I)** The bar diagrams are represented as the mean value from three independent experiments. Error bars represent SD. * $p < 0.05$.

A

bioRxiv preprint doi: <https://doi.org/10.1101/2022.11.24.517872>; this version posted November 25, 2022. The copyright holder for this preprint (which was not certified by peer review) is the author/funder. All rights reserved. No reuse allowed without permission.



B



C

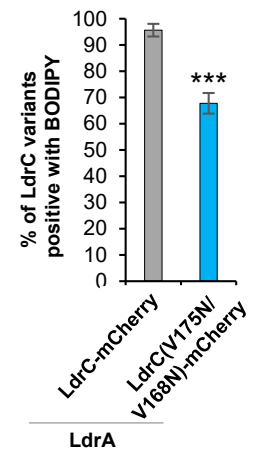


Figure 7. LD regulation from LdrC and LdrA

(A) Double deletion $ldrAldrC$ was generated by replacing $ldrC$ with sC marker was into $\Delta ldrA$. LdrA was overexpressed into $\Delta ldrA$ and $\Delta ldrC \Delta ldrA$ from heterologous $amyB$ promoter. LD number and size were analyzed using ImageJ. For LD number $n \geq 21$ hyphal areas and LD size $n \geq 145$ LD. Representative microphotographs of BODIPY-stained LD are shown. (B) Co-expression of LdrA-EGFP and LdrC variants fused with mCherry from the heterologous $amyB$ promoter. Live-cell imaging was performed from strains cultured on minimal medium with optimized carbon concentration. White and blue arrowheads represent the colocalization and no-colocalization LdrA-EGFP, respectively. The percentage of LdrA-EGFP puncta associated with LdrC-mCherry variants was calculated. $n = 19$ hyphae. (C) Co-expression of LdrA (not EGFP tagging) and mCherry-fused LdrC variants. mCherry-fused LdrC variants were stained with BODIPY and subsequent colocalization analysis. $n = 68$ LD. (A-C) Results are represented as the mean values from three independent experiments. Statistical significance was assessed using two-sampled student t -test. Error bars represent SD. ns-not significant $p > 0.05$, * $p < 0.05$, ** $p < 0.01$, *** $p < 0.001$. Bars 5 μm .

Figure 8

bioRxiv preprint doi: <https://doi.org/10.1101/2022.11.24.517872>; this version posted November 25, 2022. The copyright holder for this preprint (which was not certified by peer review) is the author/funder. All rights reserved. No reuse allowed without permission.

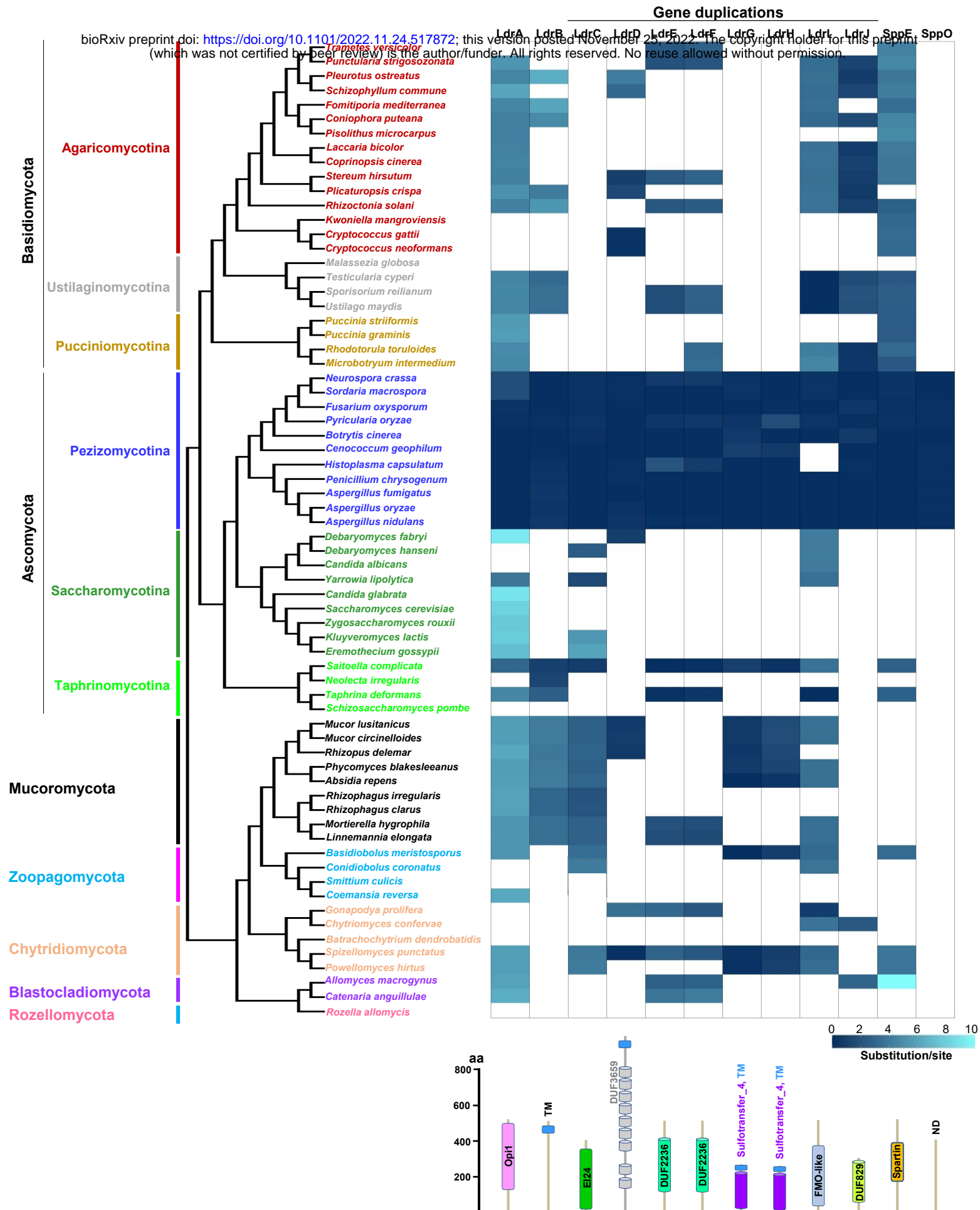


Figure 8. Conservation and divergence of LDR proteins among fungal phyla and Sub-phyla.

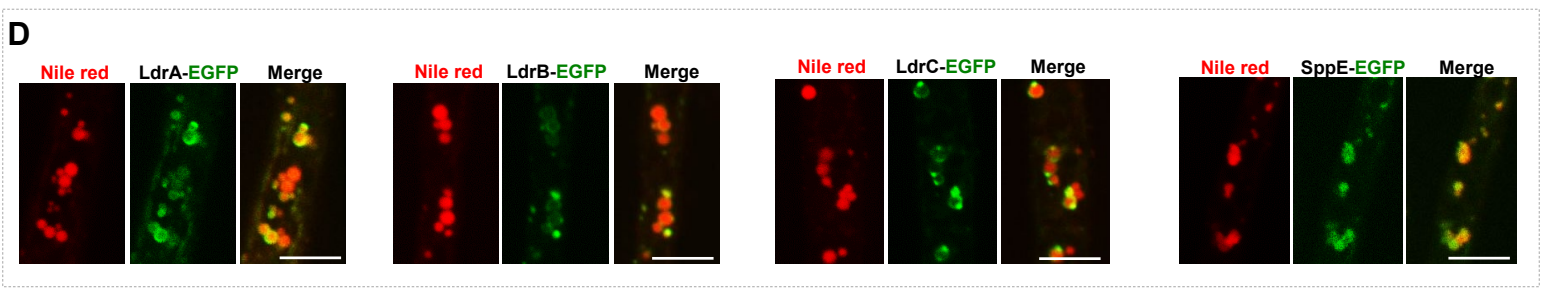
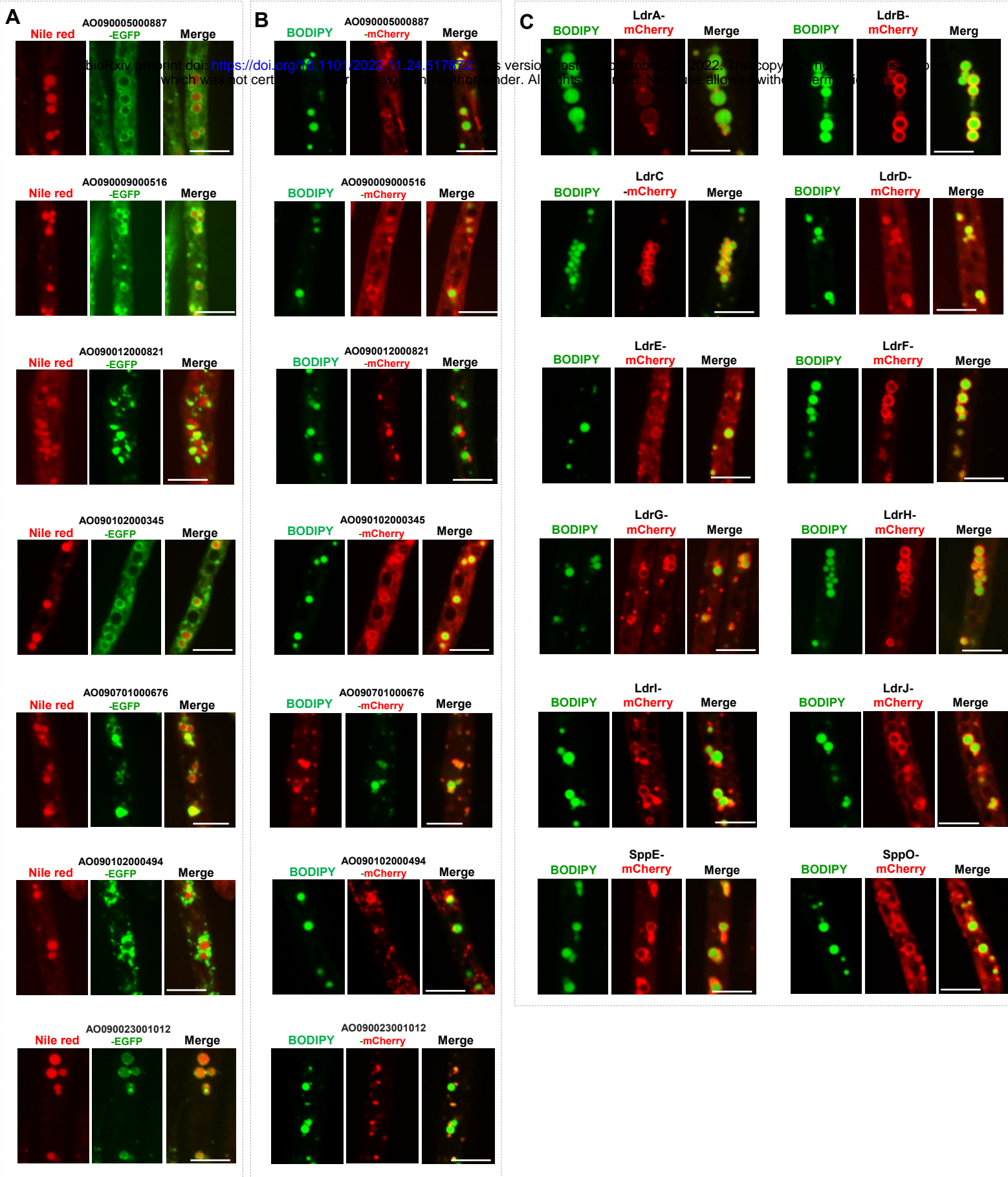
bioRxiv preprint doi: <https://doi.org/10.1101/2022.11.24.517872>; this version posted November 25, 2022. The copyright holder for this preprint (which was not certified by peer review) is the author/funder. All rights reserved. No reuse allowed without permission.

Phylogeny shows representative species from the major fungal phylum or sub-phylum. Filled and empty boxes denote the presence and absence of LDR proteins, respectively, according to the specified e-value cutoff in BLASTp (Table S2A). The scale beside the cartoons denoting protein domains at the bottom represents the number of amino acids comprising LDR proteins. (ND, no domain). Substitution rate analysis of LDR and two SPP proteins in the fungal phylum or sub-phylum from Pezizomycotina root. Amino acid substitutions per site are shown in blue as a heat map (Table S2C). A lighter shade indicates greater divergence from the Pezizomycotina.

Table 1: Amphipathicity comparison among the mutated variants of three LDR proteins

LDR proteins	Length (aa)	Variants	Hydrophobicity (<H>)	Hydrophobic moment(μH)	Hydrophobic face	Charge
LdrC	30	Wild type	0.792	0.329	MYIFVFVLLGVLL	+5
		V175N	0.731	0.273	VLLGVLL	+5
		V175N/ V168N	0.671	0.213	MYIF	+5
		V175N/ V168N/ V181D	0.604	0.162	MYIF	+4
		R173D/ K174D	0.807	0.319	MYIFVFVLLGVLL	+1
		Wild type	0.846	0.519	WVLFVLFAC	+3
		V250N	0.755	0.433	FLACPCPV	+3
LdrI	20	V250N- L254D	0.631	0.319	ACPCPV	+2
		V250N_ F261N	0.635	0.314	LACPCPV	+3
		R259D	0.857	0.508	WVLFVLFAC	+1
		Wild type	0.783	0.424	LVFVLVCPFFAALLF	+3
		V418N	0.710	0.393	PFFAALLF	+3
		V418N_ F408N	0.614	0.299	AALLF	+3
LdrB	25	V418N_ L423D	0.611	0.372	LVCPFFAAL	+2
		R420D_ R424D	0.802	0.407	LVFVLVCPFFAALLF	-1

Figure S1



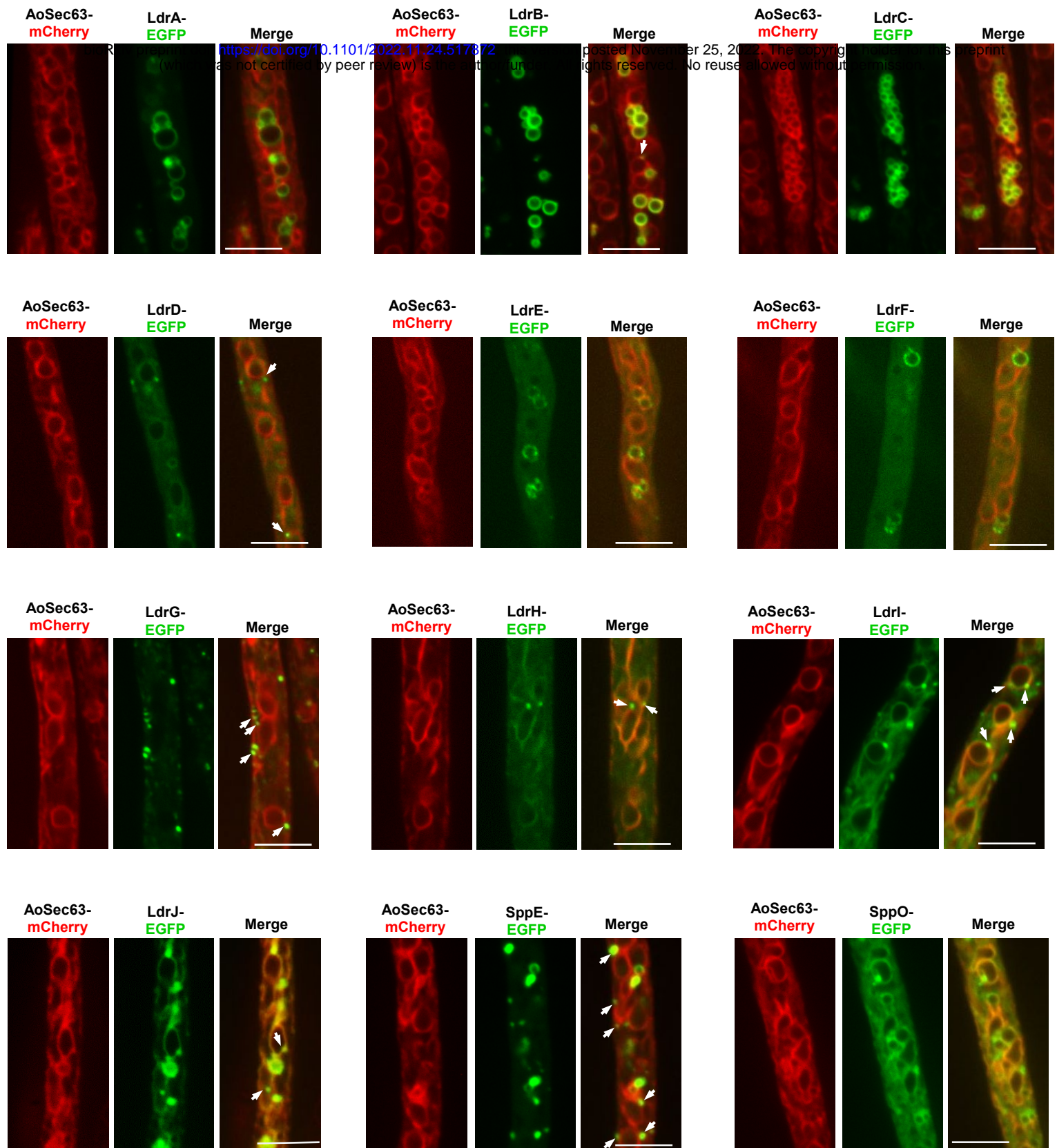
E

Figure S1. Colocalization of LD-associated proteins with LD marker dyes and ER marker proteins Sec63.

(A) Colocalization of EGFP-fused proteins with Nile red was observed from living hyphae (B) Colocalization of mCherry-fused proteins with BODIPY (C) Colocalization of mCherry-fused LDR and Spp proteins were expressed from heterologous *amyB* promoters. (D) Three LDR proteins and SppE fused with EGFP under the control of endogenous promoters were introduced in the corresponding deletion background. (B, C) Fungal hyphae were stained with 5 μM BODIPY for the visualization of LD. (A, D) LDs were visualized with 10 μg/ mL Nile red. (E) ER network was visualized with ER marker protein Sec63. EGFP-fused LDR and two SPP proteins expressed from heterologous *amyB* promoters were introduced into the strains expressing AoSec63-mCherry. Arrowheads indicate dot-like localization on the ER membrane. Representative microphotographs are shown. Bars, 5 μm.

Figure. S2

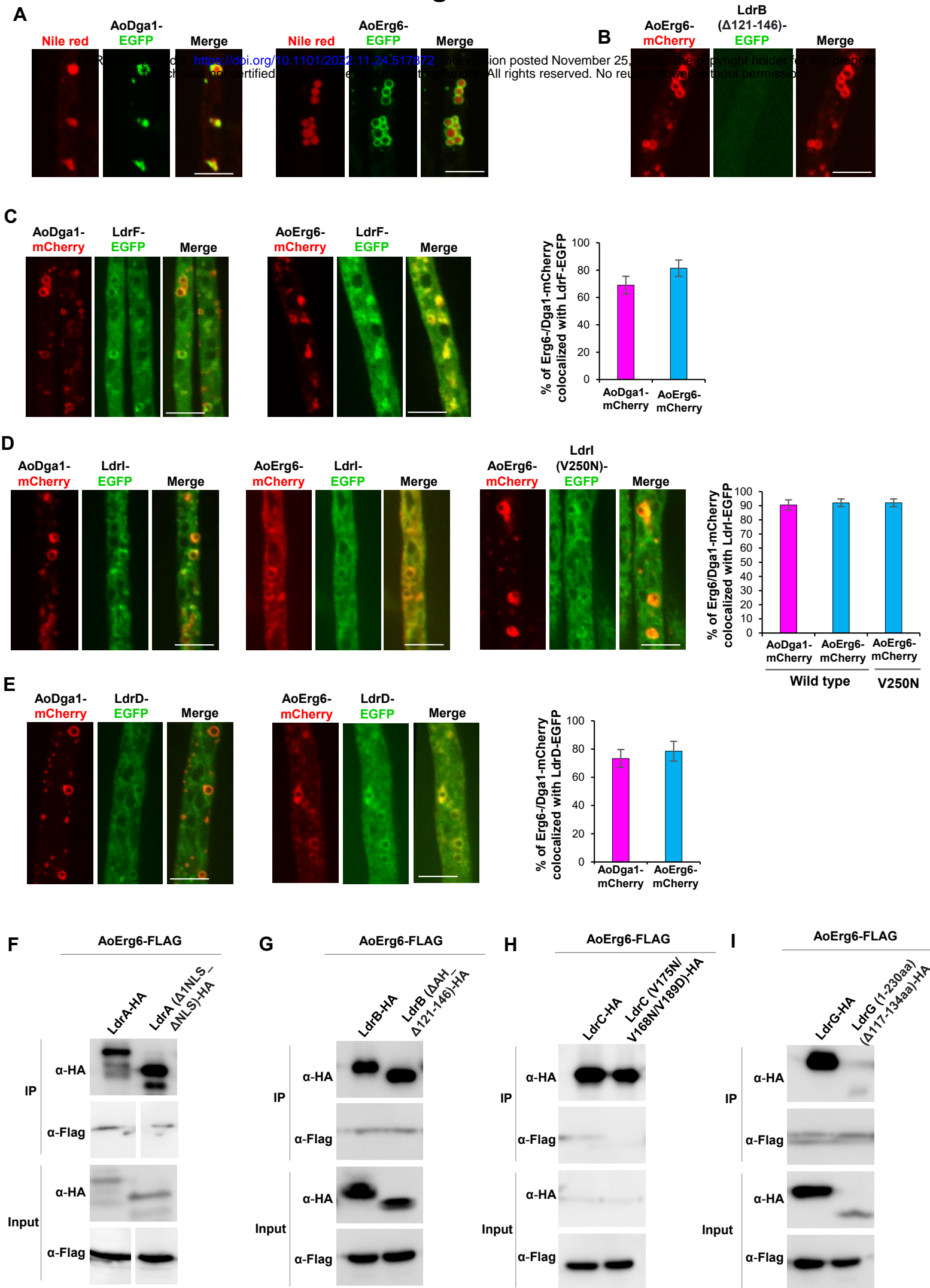


Figure S2. Colocalization and co-immunoprecipitation of several LDR proteins with LD marker proteins Erg6 and Dga1.

Aoerg6-mCherry and alternatively AoDga1-mCherry under the control of *amyB* promoter were introduced into wild-type. Previously developed EGFP-tagged LDR proteins from *amyB* promoter were further introduced onto the resultant strains. Strains were cultured on the minimal medium with optimized carbon concentration. Bars 5 μm . The percentage of AoErg6-mCherry and AoDga1-mCherry associated with EGFP-tagged LDR proteins were automatically calculated using ImageJ. Data are shown as mean \pm SD, n = 12 hyphae. **(A)** Colocalization of AoErg6-EGFP and AoDga1-EGFP with LD marker Nile red. **(B)** Colocalization of LdrB (Δ 121-146)-EGFP variant with AoErg6-mCherry. **(C)**, **(D)**, and **(E)** Colocalization of AoErg6-mCherry alternatively AoDga1-mCherry with LdrF-EGFP, LdrI-EGFP, and LdrD-EGFP, respectively. **(F–I)** LdrA, LdrB, LdrC, and LdrG did not physically interact with AoErg6. Coimmunoprecipitation analysis between AoErg6 and four LDR proteins was performed. Analyzed LDR proteins fused with HA from heterologous *amyB* promoters were introduced into the corresponding deletion backgrounds. Aoerg6-FLAG was further ectopically introduced into resultant strains. Along the wild-type variants, AH disrupting mutants or truncations were used to distinguish whether the precipitation is LD specific. After grinding mycelial powder, cell lysates were incubated in the buffer containing detergent NP-40. IP was performed with anti-HA antibodies. The samples were analyzed by immunoblotting with the indicated antibodies. **(F)**, **(G)**, **(H)**, and **(I)** interaction analysis between AoErg6-Flag and LdrA-HA, LdrB-HA, LdrC-HA, and LdrG-HA, respectively.

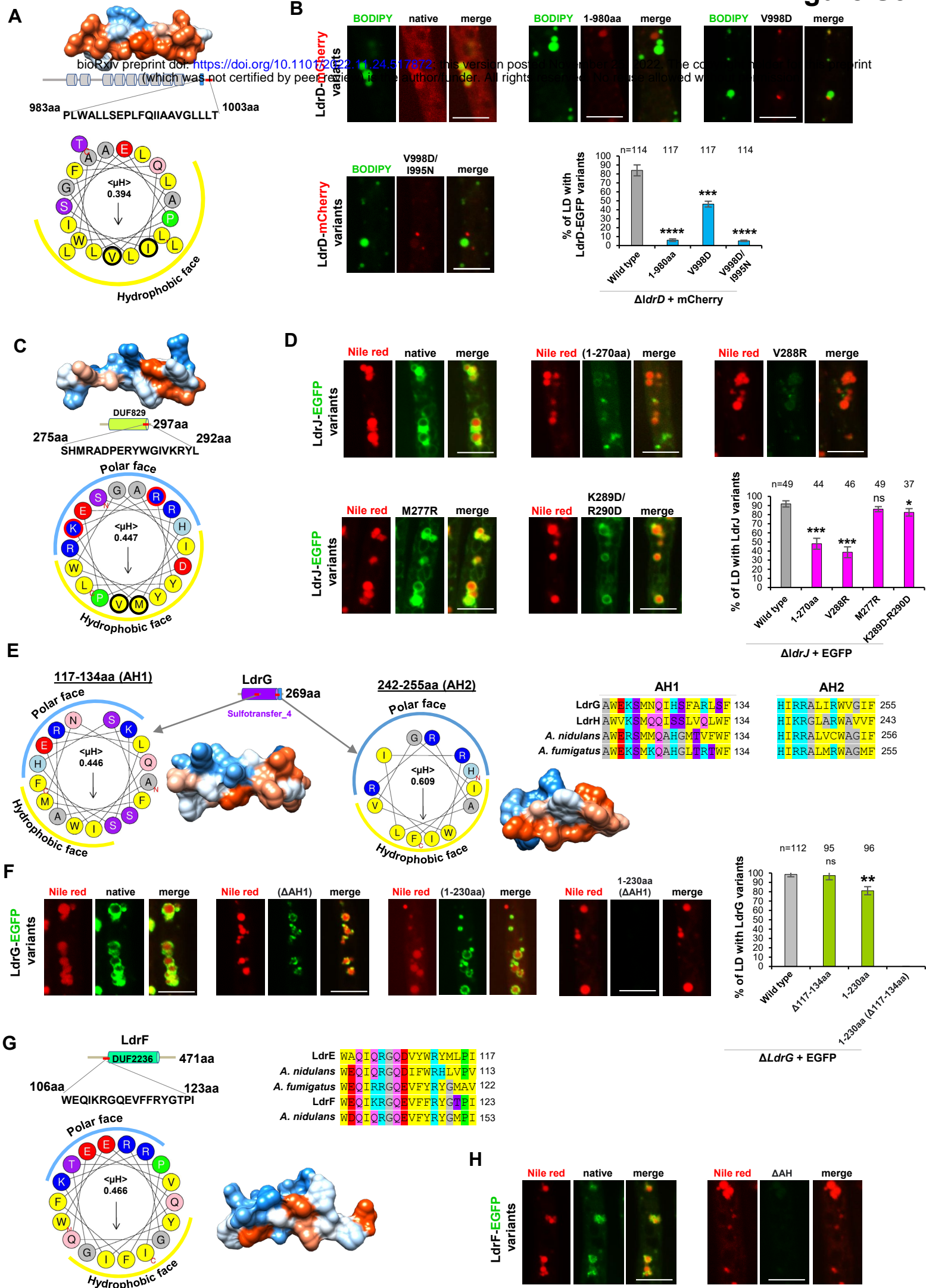


Figure S3. LdrD, LdrJ, LdrG, and LdrF bind to LD surface through the predicted AHs

(A), (C), (E), and (G) helical wheels and 3D model of α -helical representation of predicted AH. Amino acid properties and positions are indicated by colors and numbers, respectively. Hydrophobic and polar faces are shown with orange and blue curve lines, respectively. (E) Multiple sequence alignment among the paralogues and orthologues of LdrG covering two regions predicated as AHs. (G) Multiple sequence alignment among the paralogues and orthologues of LdrF covering two regions predicted as AH. (B), (D), (F), and (H) $\Delta ldrD$, as well as $\Delta ldrJ$, $\Delta ldrG$, and $\Delta ldrF$ were complemented with mCherry as well as EGFP-fused corresponding wild-type and AH-disrupting mutational variants, respectively, from heterologous *amyB* promoter. strains cultured on the minimal medium were stained with BODIPY (B) or Nile red (D, F, and H) in live hyphae. Representative microphotographs are shown. Bars 5 μ m. The percentage of BODIPY or Nile red stained-LD positive with LdrD, LdrJ, and LdrG variants was counted manually. Experiments were done in triplicates. Statistical significance was assessed using two-sampled student *t-test*. Error bars represent SD. ns-not significant $p > 0.05$, * $p < 0.05$, ** $p < 0.01$, *** $p < 0.001$, **** $p < 0.0001$.

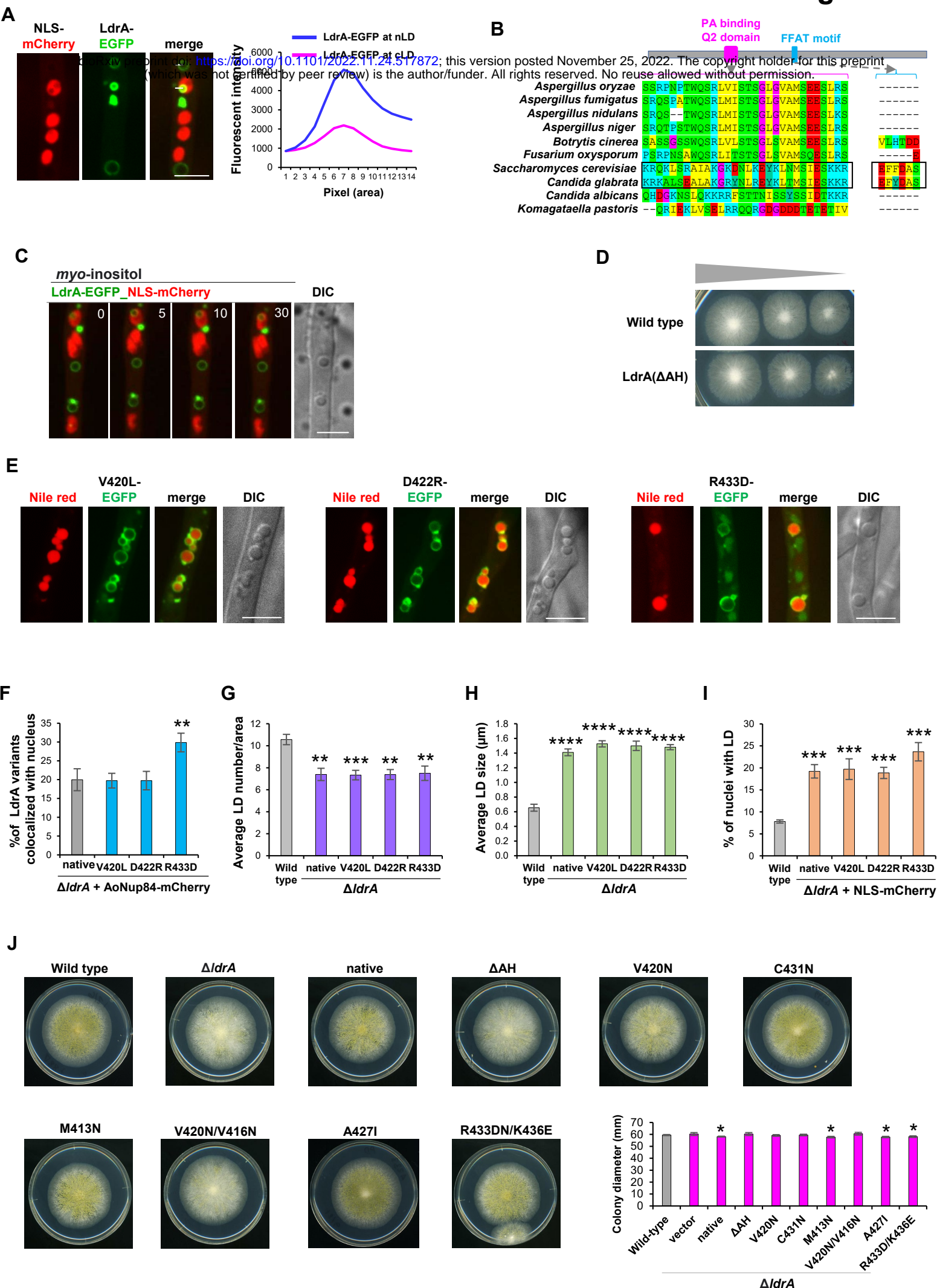
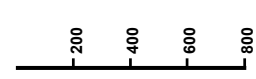


Figure S4. Phylogenetic and physiological difference of LdrA from that Opi1 of budding yeast as well as its LD binding affinity via AH.

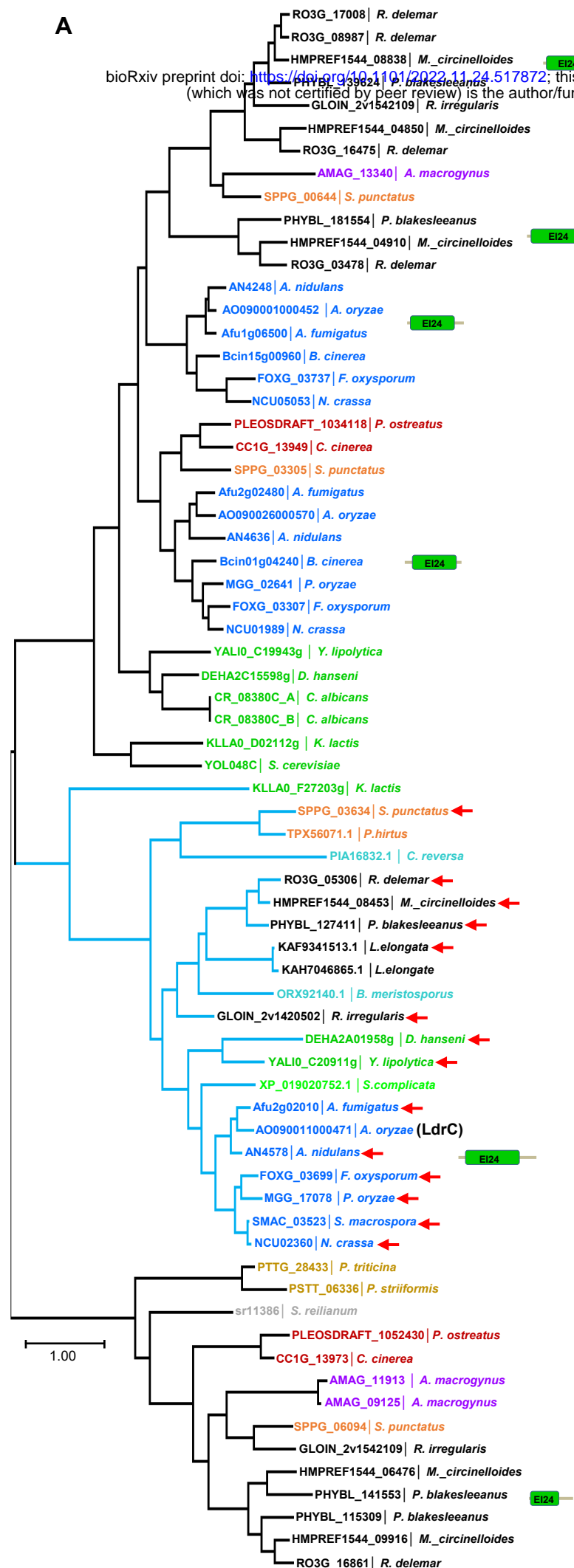
(A) Colocalization analysis of LdrA-EGFP and NLS-mCherry reveals high affinity binding of LdrA to nLD over cLD. Y axis of the line graph presents the mean fluorescent intensity of LdrA-EGFP on LD. **(A)** and **(D)** strains were cultured in CD agar medium supplemented with 1% casamino acids for 20 h. Bars 5 μ m. **(B)** Drawing of the domain organization of budding-yeast Opi1 and its binding feature on ER membrane using Q2 domain, as well as FFAT motif. Upon the addition of inositol, Opi1 disassociates from ER and translocates into the nucleus. **(C)** Multiple sequences alignment of the Q2 domain and FFAT motif among the fungal orthologues shows a high degree of sequence divergence. Alignment was performed using ClustalW. **(D)** LD binding of LdrA was independent of the presence of the excessive amount of inositol provided in the medium. After 20 h of growth, the culture was treated with 200 μ M of myoinositol. Times= min and Bars 5 μ m. **(E)** LdrA variant solely localized at the nucleus did not show inositol auxotrophy. Strains were cultured in CD agar in the absence of inositol for 2 d. **(F)** Percentage of nucleus positive with LdrA variants. n \geq 212 nuclei **(G-H)** Quantification of average LD number (per area) and average LD size from LdrA variants (no EGFP tagging), respectively. **(G)** n \geq 21 hyphal area and **(H)** 133 LD. **(I-J)** Percentage of nuclei positive with LDs. n \geq 160 nuclei. **(F-I)** Bar diagrams are presented as the mean value from three independent experiments. Statistical significance was assessed using two-sampled student *t-test*. Error bars represent SD. ns-not significant p > 0.05, *p < 0.05, **p < 0.01, ***p < 0.001, ****p < 0.0001 **(J)** Reduced conidiation and reduced colony growth in strains with defective and overactive, respectively in LD biogenesis. A conidial suspension (10⁴ conidia in 4 μ l water solution) of the strains was spotted on PD media and cultured for 4 d.

Figure S5

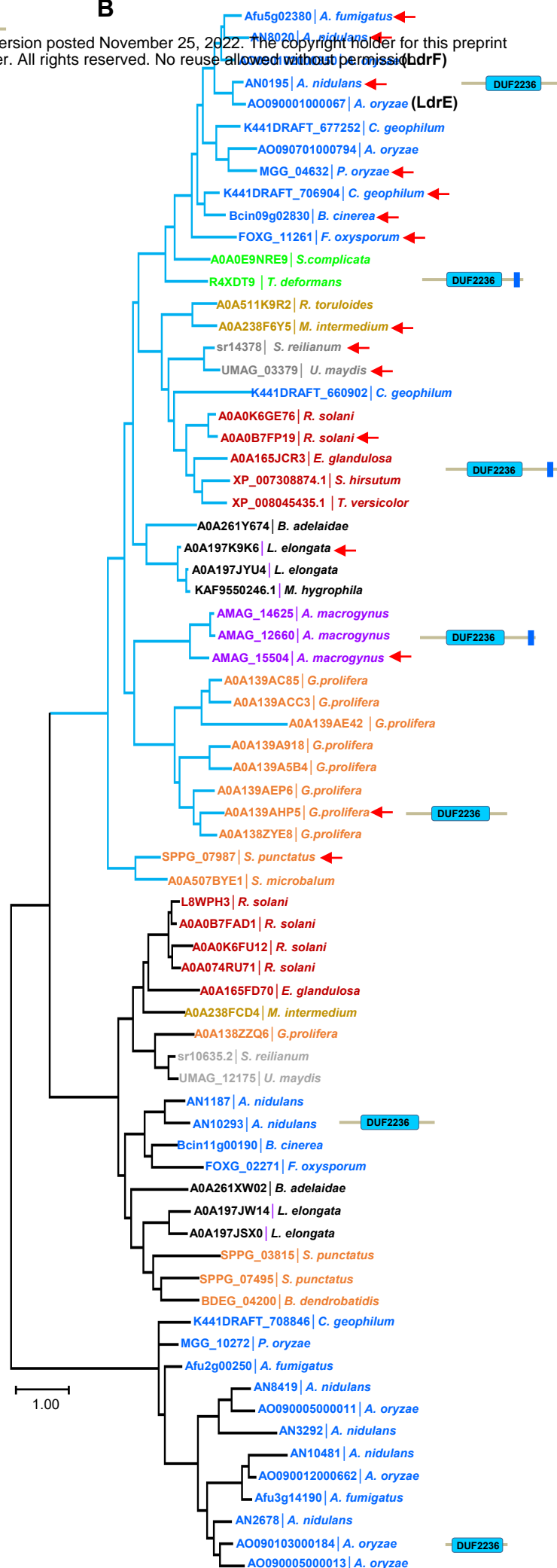


A

bioRxiv preprint doi: <https://doi.org/10.1101/2022.11.24.517872>; this version posted November 25, 2022. The copyright holder for this preprint (which was not certified by peer review) is the author/funder. All rights reserved. No reuse allowed without permission.

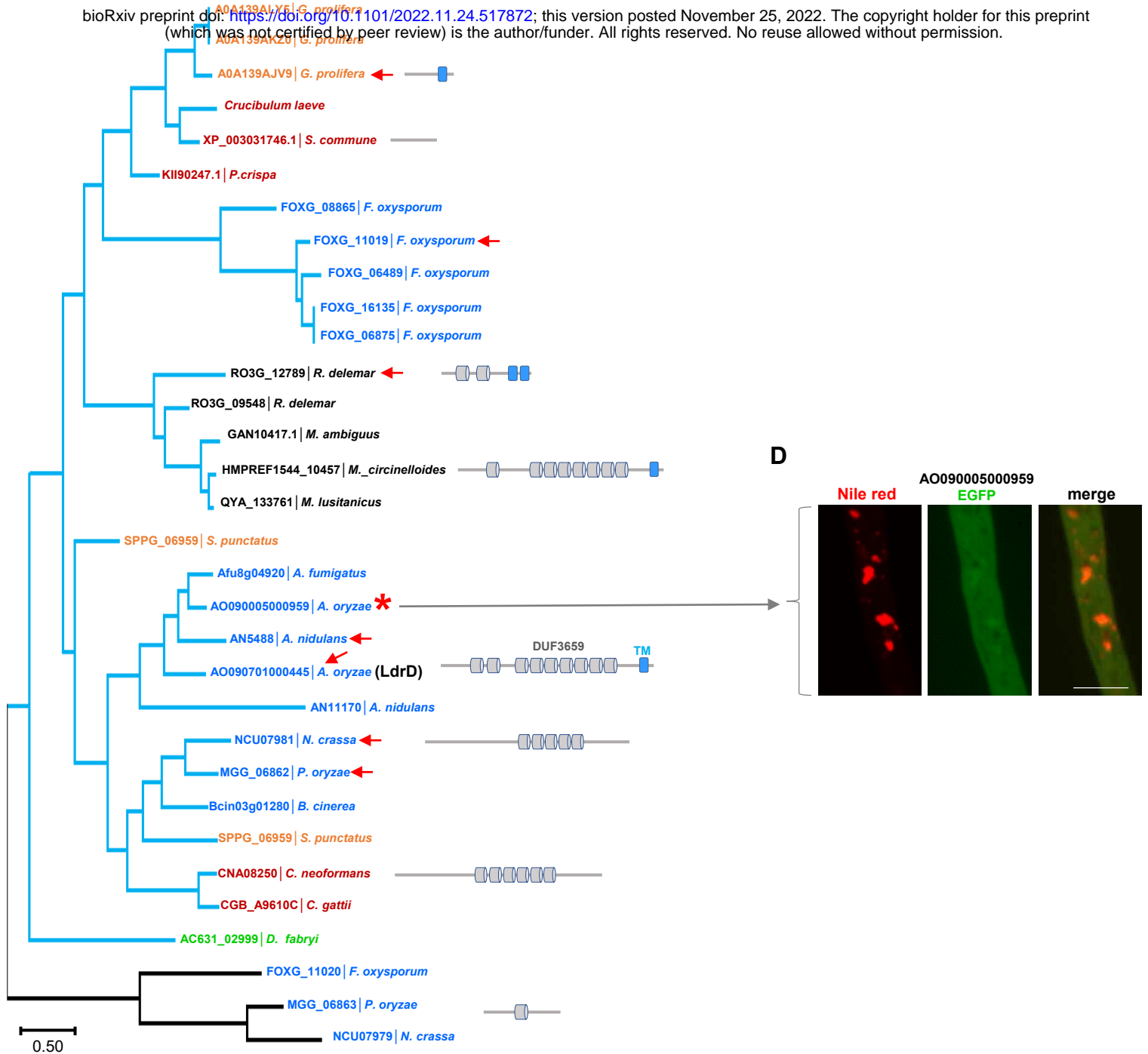


B

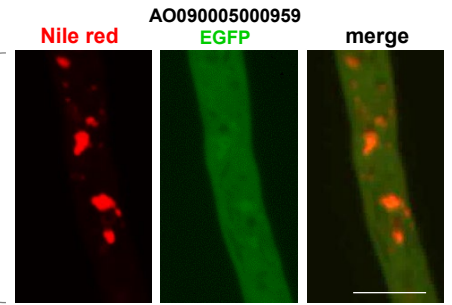


C

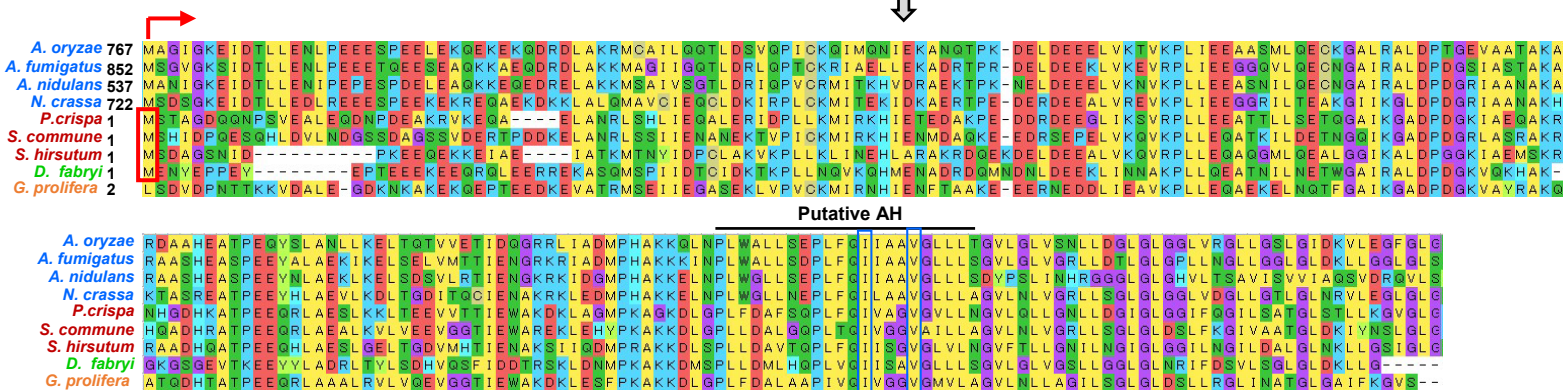
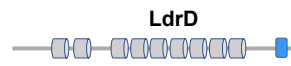
bioRxiv preprint doi: <https://doi.org/10.1101/2022.11.24.517872>; this version posted November 25, 2022. The copyright holder for this preprint (which was not certified by peer review) is the author/funder. All rights reserved. No reuse allowed without permission.



D

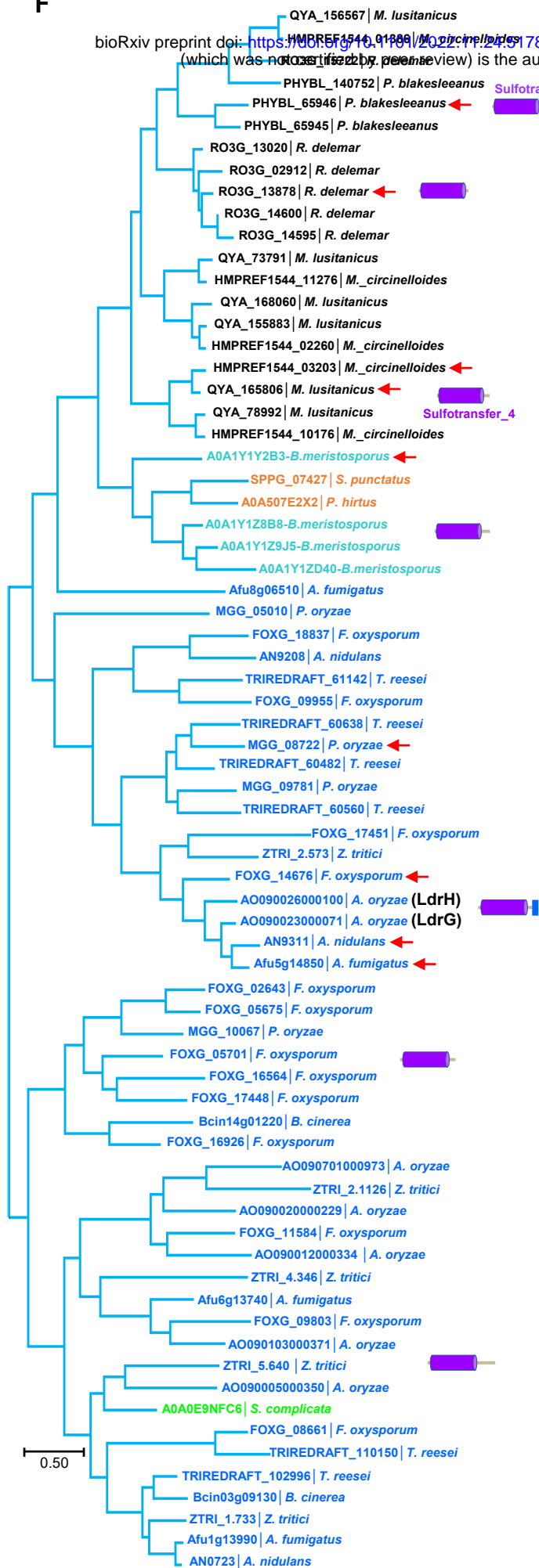


E

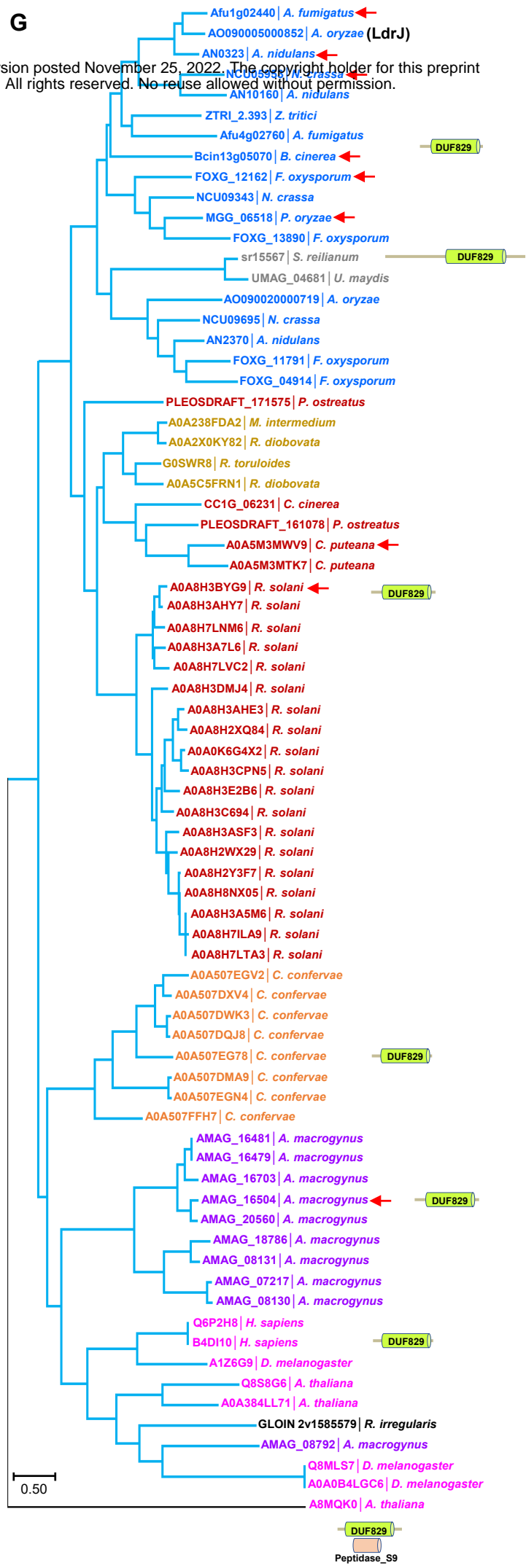


F

bioRxiv preprint doi: <https://doi.org/10.1101/2022.11.24.517872>; this version posted November 25, 2022. The copyright holder for this preprint (which was not certified by peer review) is the author/funder. All rights reserved. No reuse allowed without permission.



G



H

bioRxiv preprint doi: <https://doi.org/10.1101/2022.11.24.517872>; this version posted November 25, 2022. The copyright holder for this preprint (which was not certified by peer review) is the author/funder. All rights reserved. No reuse allowed without permission.

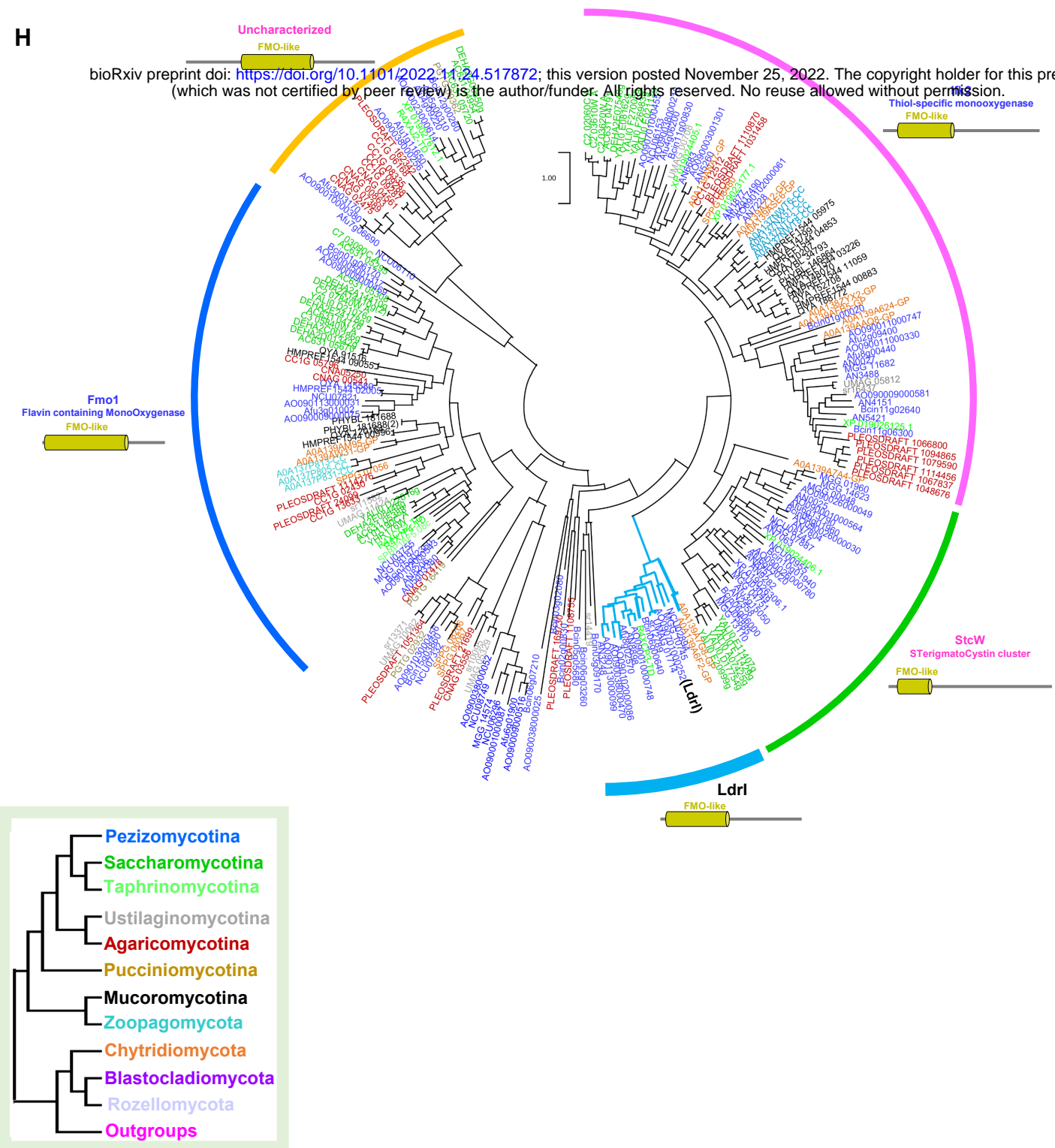


Figure S5. Phylogenetic tree of eight LDR proteins possibly evolved by gene duplications. Domains were predicted using the simple modular architecture research tool (SMART) and cross-checked with NCBI. Total proteins containing the analyzed domain within the given species were retrieved from FungiDB genome database and case dependently from UniProt (See Methods). Maximum-likelihood trees were constructed using Mega 11. Diagrams of protein domain structures are shown with the respective clades. The probable orthologous clades are represented by the blue color branches of the tree. In multiple proteins with the same domain, red arrowheads indicate the proteins used for the substitution rate analysis in Fig. 8. (A) Phylogeny of fungal proteins having EI24 present in LdrC. (B) Phylogeny of fungal proteins having DUF2236 domain present in LdrE and LdrF. (C) Phylogeny of fungal proteins having DUF3659 domains in LdrD. Star mark represents the paralogues of LdrD. (D) AO90005000959 fused with EGFP was ectopically expressed into the wild-type. LD was visualized with Nile red. Bars 5 μ m. (E) Multiple sequence alignment shows the conserved C-terminal region and highlights the residues critical for amphipathic helices organization. (F) Phylogeny of fungal proteins having Sulfotransfer_4 domains in LdrG and LdrH. (G) Phylogeny of fungal proteins containing DUF829 domains present in LdrJ. (H) Phylogeny of fungal proteins containing FMO-like domains present in LdrI. Gene names ending in CC, GP, and TD indicate *Conidiobolus coronatus*, *Gonapodya prolifera*, and *Taphrina deformans*, respectively.